

# Multicomponent chiral quantification with UV circular dichroism spectroscopy: ternary and quaternary phase diagrams of Levetiracetam

---

**Maxime D. Charpentier<sup>1</sup>, Raghunath Venkatramanan<sup>1</sup>, Céline Rougeot<sup>2</sup>, Tom Leyssens<sup>3</sup>, Karen Johnston<sup>4</sup>, Joop H. ter Horst<sup>1,5</sup>**

1. EPSRC Centre for Innovative Manufacturing in Continuous Manufacturing and Crystallization (CMAC), University of Strathclyde, Technology and Innovation Centre, 99 George Street, Glasgow G1 1RD, U.K.

2. UCB Pharma SA, chemin du Foriest, 1420 Braine-L'Alleud, Belgium

3. Institute of Condensed Matter and Nanosciences, UCLouvain, Place L. Pasteur 1, Belgium.

4. Department of Chemical and Process Engineering, University of Strathclyde, James Weir Building, 75 Montrose Street, Glasgow G1 1XJ, U.K.

5. Univ Rouen Normandie, Laboratoire Sciences et Méthodes Séparatives (SMS), UR 3233, F-76000 Rouen, France

## Abstract

---

Chiral molecules are challenging for the pharmaceutical industry because, although physical properties of the enantiomers are the same in achiral systems, they exhibit different effects in chiral systems, such as the human body. The separation of enantiomers is desired but complex, as enantiomers crystallize most often as racemic compounds. A technique to enable the chiral separation of racemic compounds is to create an asymmetry in the thermodynamic system by generating chiral cocrystal(s) using a chiral coformer and using the solubility differences to enable separation through crystallization from solution. However, such quaternary systems are complex and require analytical methods to quantify different chiral molecules in solution. Here we develop a new chiral quantification method using Ultraviolet-Circular Dichroism spectroscopy and multivariate Partial Least Squares calibration models, to build multicomponent chiral phase diagrams. Working on the quaternary system of (R)- and (S)-2-(2-oxopyrrolidin-1-yl)butanamide enantiomers with (S)-mandelic acid in acetonitrile, we measure accurately the full quaternary phase diagram for the first time. By understanding the phase stabilities of the racemic compound and the enantiospecific cocrystal, the chiral resolution of levetiracetam could be designed due to a large asymmetry in overall solubility between both sides of the racemic composition. This new method offers improvements for chiral molecule quantification in complex multicomponent chiral systems and can be applied to other chiral spectroscopy techniques.

## 1. Introduction

---

Because of their mirror image symmetry, enantiomers exhibit the same enantiopure physical properties, such as crystal melting point, solubility, molecular reactivity with achiral molecules, and the same response in analysis by conventional spectroscopy methods (NMR, UV, IR).<sup>1</sup> However, their interaction with chiral systems, for example a chiral drug interacting with chiral receptors in the human body, differs and hence induces different biological activities. In many cases, one enantiomer has a desired therapeutic effect while the other may have no effect or even a harmful effect.<sup>2-5</sup> In addition, a non-active counter-enantiomer is an impurity that can constitute up to 50% of the product, which has economic consequences.<sup>6</sup> This is the case for (S)-2-(2-oxopyrrolidin-1-yl)butanamide, known commonly as levetiracetam, a nootropic drug used as an anticonvulsant to treat epilepsy.<sup>7</sup> Although the pure enantiomer product is desired for chiral drugs, the process of obtaining enantiopure active pharmaceutical ingredients (APIs), called chiral resolution, is challenging. Many chiral molecules are synthesized by non-stereoselective chemical reactions, leading to racemic mixtures that require separation. Crystallisation is the preferred strategy at industrial scale as it is relatively inexpensive<sup>8, 9</sup> and can be highly selective depending on the solid-liquid equilibria between enantiomers in solution.<sup>1, 10</sup> In 5-10% of cases, enantiomers crystallize separately to form a conglomerate, which is a physical mixture of enantiopure crystals that is amenable to chiral resolution processes.<sup>11-21</sup> However, in 90-95% of cases a racemic crystal is formed and chiral resolution through crystallization is difficult or even impossible.<sup>1, 22, 23</sup> An alternative resolution method is to generate multicomponent crystals. If chiral molecules can be ionized, Pasteurian resolution<sup>24-26</sup> is possible by formation of diastereomeric salts with a resolution agent. Otherwise, a conglomerate of enantiopure cocrystals or solvates can emerge using an achiral coformer or a solvent.<sup>27-29</sup> Finally, using a chiral coformer can either induce formation of a diastereomeric pair of enantiopure cocrystals, or an enantiospecific cocrystal.<sup>30-36</sup>

Understanding these multicomponent systems requires the acquisition of accurate phase diagrams that are key to designing robust and reliable crystallization processes,<sup>37, 38</sup> especially for chiral molecule separations.<sup>25, 39</sup> Phase diagrams represent compositional phase domains for equilibrium states of a system. The equilibrium state is strongly dependent on the system's intensive properties, such as temperature and overall component compositions. However, phase diagrams become more complex as the number of components increases. In the case of chiral resolution by crystallization, ternary phase diagrams are commonly used to understand the solid-liquid equilibria between enantiomers in a solvent,<sup>35, 36, 40-42</sup> a single enantiomer with a salt-former or a coformer,<sup>31, 35, 36, 43</sup> and diastereomeric salts systems.<sup>25, 26</sup> However, to truly understand and optimize a chiral resolution process of a racemic compound with a chiral coformer (or salt-former) in a solvent,<sup>31, 35, 36, 44</sup> it is necessary to know the quaternary phase diagram.

Multicomponent chiral phase diagrams increase in complexity as the number of chiral components increases because of the difficulty in quantifying them. For instance, the study of two symmetrical enantiospecific cocrystals requires the quantification of four chiral molecules in a solvent to determine the phase diagrams.<sup>45</sup> Therefore, accurate quantitative methods to measure the concentration of all chiral molecules and to distinguish between two enantiomers are needed. Chiral quantification methods usually involve first measuring the components' total concentration using

gravimetry,<sup>40</sup> titration,<sup>41</sup> UV-Vis spectroscopy<sup>46</sup> or achiral HPLC,<sup>36</sup> and then quantifying the enantiomer's concentrations using polarimetry<sup>47</sup> or chiral HPLC.<sup>23, 40</sup> Polarimetry can only characterize a single variable variation, making quantification unreliable if more than one pair of enantiomers is present,<sup>48</sup> and also presents issues such as low sensitivity, and influence by other components and temperature variation.<sup>49, 50</sup> Chiral HPLC does not have these disadvantages and is more widely used. It can quantify two enantiomers in a single step,<sup>23, 42, 51</sup> and for non-enantiomeric chiral molecules, quantification can be designed with both achiral and chiral HPLC methods.<sup>35, 52</sup> However, quantification of two enantiomers and at least one other chiral molecule increases the complexity of finding chromatography separation conditions. A combination of two different methods, such as achiral and chiral HPLC, often becomes necessary.<sup>36, 45, 53</sup> The requirement for multiple chromatography columns and mobile phases becomes a disadvantage, as new HPLC methods need to be developed for every chiral multicomponent system studied.<sup>54</sup>

An interesting alternative to analyse chiral molecules is Circular Dichroism (CD). This technique is based on the differential interaction of a chiral molecule with left and right circularly polarized light (Figure 1) and is commonly used for structure and conformation determination of chiral molecules and proteins.<sup>55-57</sup> Ultraviolet circular dichroism (UV-CD) is CD in UV wavelengths and has proven its efficiency to quantify enantiomers in solution.<sup>58-61</sup> Two signals are measured simultaneously: one is the UV signal that depends on all the molecules dissolved, and one is the CD signal that depends on the differential concentrations between the chiral compounds present. The advantage of UV-CD is that it can simultaneously detect more than one pair of enantiomers with a high sensitivity.<sup>57, 62</sup> The signals depend on component interactions in their spectroscopic behaviour across a range of wavelengths. With the use of chemometrics<sup>63-66</sup> for data analysis, complex spectra can be understood. The composition information can be linked to the spectra to develop robust calibration models allowing unknown solutions to be quantified. Indeed, chemometrics on absorption spectroscopy rely on the Beer-Lambert law,<sup>67, 68</sup> a proportionality relation between absorbance and concentration at every wavelength measured. Therefore, multivariate methods consider the different wavelength variables to quantify the system with improved accuracy.<sup>69</sup> Previous quantification work with CD used a two-step approach with Multivariate Curve Resolution (MCR) to decompose datasets into individual component spectra and estimate their relative contributions, that are later transformed into absolute trends by fitting known values and performing a two-point calibration.<sup>70</sup>



**Figure 1:** Circular Dichroism: a light source composed of an equal amount of left-handed (blue) and right-handed (red) circularly polarized light, one of which is preferentially absorbed by a chiral molecule. A differential absorbance  $\Delta A$  is measured between absorbance of left-handed light  $A_L$  and right-handed light  $A_R$ .

In this study, we propose a new approach with multivariate partial least squares (PLS) calibration models<sup>71, 72</sup> to quantify chiral multicomponent systems using UV-CD spectroscopy. With

this method, we determine chiral phase diagrams in the quaternary system of 2-(2-oxopyrrolidin-1-yl)butanamide enantiomers (R and S), (S)-mandelic acid (S-MA) and acetonitrile (MeCN) at 9°C. This system was previously found to have stable solid phases of the pure solutes, a stable racemic compound between enantiomers, and an enantiospecific 1:1 cocrystal between S and S-MA.<sup>31, 36</sup> The ternary phase diagrams of this system have until now only been estimated using limited data acquired from a combination of HPLC methods.<sup>36</sup> In this work, we first present a reevaluation of the latter data with our method and propose a more accurate representation of the ternary phase diagrams. Then, we construct the full isothermal quaternary phase diagram for the first time, by acquiring many solubility data inside the tetrahedron plot. With the understanding of the solid phase stability and the influence of component compositions on their solubility, the chiral resolution of levetiracetam by enantioselective cocrystallization can be designed from the phase diagram data.

## 2. Experimental methods

### 2.1. Materials

To distinguish components in the following study, the 2-(2-oxopyrrolidin-1-yl)butanamide enantiomers will be labelled **R** and **S**, and their racemic compound **RS**, the coformer S-mandelic acid **S-MA**, the enantiospecific cocrystal **S:S-MA**, and the solvent acetonitrile **MeCN** (Figure 2). The commonly known names are levetiracetam for S and etiracetam for RS. Levetiracetam is the biologically active enantiomer, and is a medication used to treat epilepsy. R, S and RS were provided by UCB Pharma. S-MA ( $\geq 99\%$ , Sigma-Aldrich) and MeCN (HPLC grade, 100%, VWR Chemicals) were used as received. S:S-MA was crystallized by slow evaporation of a 1:1 molar ratio solution in methanol (MeOH) and confirmed by XRPD. The XRPD patterns of materials used, and their references can be found in Supplementary Information (Section S1). All solid phases present specific diffraction peak positions that permit assessment of their presence in solid mixtures.

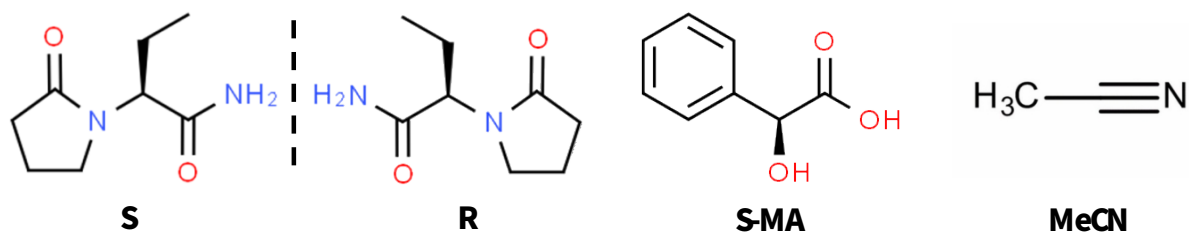


**Figure 2:** Chemical structures of the four components levetiracetam S (antiepileptic drug), its counter enantiomer R, S-mandelic acid (S-MA) and the solvent acetonitrile (MeCN).

### 2.2. X-Ray Powder Diffraction (XRPD)

XRPD analyses were performed using a Bruker D8 Advance II diffractometer with Debye-Scherrer transmission from a Cu source radiation ( $1.541 \text{ \AA}$ ) with an operating voltage of 40kV, current 50mA,  $\text{K}\alpha 1$  Johansson monochromator and 1mm anti-divergence slit. A Bruker D2 Phaser diffractometer was also used, with Bragg-Brentano reflection  $\theta/\theta$  geometry from a Ni filtered Cu source radiation ( $1.541 \text{ \AA}$ ) with an operating voltage of 30kV, current 10mA and 0.2mm anti-divergence slit. A scanning range of  $2\theta$  values from  $4^\circ$  to  $35^\circ$  was applied with a  $0.017^\circ$  step and a step time of 1s.

### **2.3. Ultraviolet Circular Dichroism (UV-CD) spectroscopy**

UV-CD spectroscopy was performed using a Chirascan-Plus spectrometer from Applied Photophysics, constantly purged with a nitrogen flow. The samples were analysed in a Hellma quartz cell with a 0.1 mm path length. Both UV and CD spectra were collected with a 0.5 nm step and 1 second per point in the 200-260 nm range. The background of pure acetonitrile was measured and automatically subtracted from the spectra using the instrument software. As the detector is saturated when solutions with a total concentration of dissolved components exceed 5mg/mL, the calibration range is set from 0.5 to 5mg/mL, and all samples were diluted to fall into this calibration range. The UV and CD spectra are expressed in, respectively, absorbance units and ellipticity units ( $\theta$ ), a value proportional to circular dichroism. The data were collected using Chirascan Pro data V4.4.2.0 and the analysis of the UV-CD data was done using Origin Pro 2017 and Pls\_toolbox 4.0 by Eigenvector research Inc. The spectra of both UV and CD were pre-processed with first derivative baseline correction followed by Savitzky-Golay smoothing<sup>73</sup> of second order polynomial with five window points, and mean centring.<sup>74</sup> The spectra were otherwise free of artefacts and baseline issues, so no additional pre-processing was done.

### **2.4. Development of a multivariate calibration for quantification**

#### **2.4.1. Calibration samples**

A multivariate calibration model using samples of known composition, i.e. calibration samples, was developed to allow the measurement of unknown composition solutions from UV-CD spectra. The chosen independent variables in the 4-component calibration samples are the mass fraction  $x$ , for R ( $x_R$ ), S ( $x_S$ ) and S-MA ( $x_{S-MA}$ ), with the solvent MeCN mass fraction  $x_{MeCN} = 1 - x_R - x_S - x_{S-MA}$ . The construction of the model was to allow quantification of equilibrated samples from a quaternary phase diagram, which is a tetrahedron plot whose triangular faces are isothermal ternary phase diagrams. The calibration space therefore was designed to cover the entire quaternary space, consisting of the perimeter and the interior of the tetrahedron. Experimental solvent free component ratios of the calibration samples are shown in Figure 3. Each ratio (square) represents five calibration samples prepared by successive dilutions of the same bulk solution within the UV-CD calibration range of the molecules (0.5 to 5mg/mL total concentration), allowing the total concentration for all components to be covered accurately. This calibration sample preparation method yields a calibration data set with 270 compositions. The 270 calibration sample compositions can be found in the Supplementary Information (Table S1). For each calibration sample UV and CD spectra were measured.

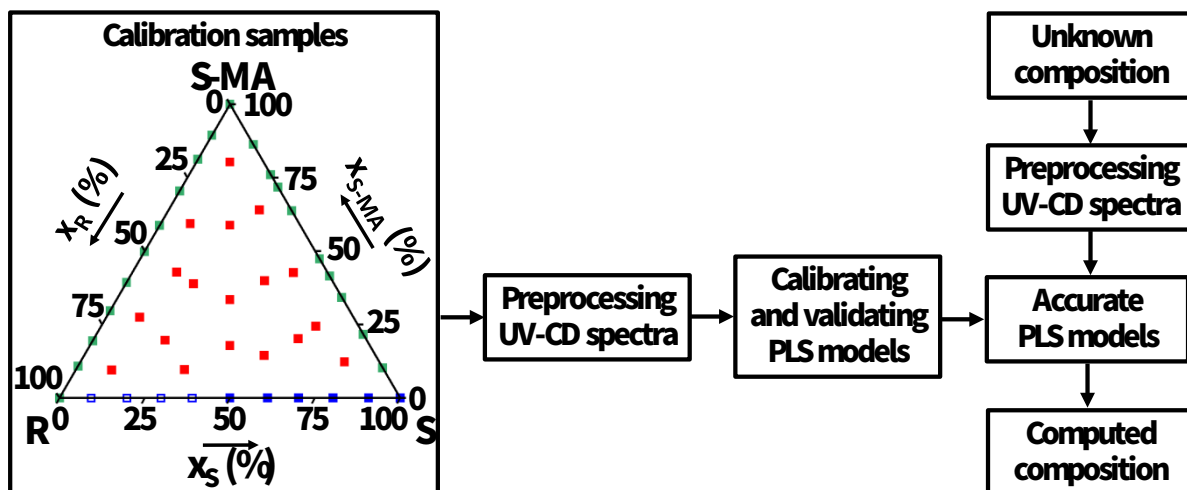


**Figure 3:** Design of the multivariate calibration, with calibration samples as input, to obtain PLS models allowing the computation of unknown compositions from their UV-CD spectra. The distribution of calibration samples is represented by their solvent free mass fraction in components. For each fraction, five solutions of varying total concentration were prepared from successive dilutions into the UV-CD calibration range (0.5 to 5 mg/mL), and the related UV and CD spectra were measured and gathered to build the model. Blue points correspond the R/S/MeCN ternary section, open squares being obtained from symmetry of the experimental CD spectra with S being in excess. Green points correspond to ternary sections S/S-MA/MeCN and R/S-MA/MeCN. Red points correspond to quaternary compositions containing R, S, and S-MA in MeCN.

#### 2.4.2. Design of multivariate partial least squares (PLS) calibration models

The modelling for quantitative determination of  $x_R$ ,  $x_S$  and  $x_{S-MA}$  in unknown solutions, using experimental UV and CD spectra (see Figure 3), requires a calibration using UV and CD spectra of the calibration samples. Here, we use a multivariate partial least square (PLS) calibration.<sup>71, 72</sup> Two calibration models were designed, one for the UV data and the other for CD data. Both types of signals are influenced differently by the concentration in all dissolved components (R, S or S-MA). They both follow the Beer-Lambert proportionality law<sup>67, 68</sup> between absorbance and concentration at every wavelength measured. For UV spectra, because R and S absorb UV identically, two variables were defined as influencing the signal in the calibration: the total enantiomer mass fraction  $x_{S+R}=x_S+x_R$  and the S-MA mass fraction  $x_{S-MA}$ . However, for CD the two enantiomers R and S have a symmetrical response and the spectra depend on the differential mass fraction  $x_{S-R}=x_S-x_R$  between enantiomers. Therefore, two variables were defined as influencing the CD spectra in the calibration: the differential mass fraction between enantiomers  $x_{S-R}$  and the mass fraction in S-MA  $x_{S-MA}$ . With  $x_{S+R}$  and  $x_{S-R}$  from UV and CD data, the enantiomeric excess

$$E = \frac{x_S - x_R}{x_S + x_R} = \frac{x_{S-R}}{x_{S+R}}$$

was computed and  $x_R$  and  $x_S$  were retrieved as

$$x_S = \frac{1 + E}{2} * x_{S+R}$$

and

$$x_R = x_{S+R} - x_S$$

Since only one enantiomer of mandelic acid (S-MA) is present, both UV and CD calibration models yield the total S-MA concentration  $x_{S-MA}$ .

After their acquisition, all spectra were pre-processed (Figure 3) by first derivative baseline correction followed by Savitzky-Golay smoothing<sup>73</sup> of second order polynomial with five window points, and mean centring.<sup>74</sup> This maintains the shape of the spectra and allows separation between the peaks and removal of artefacts, such as baseline shifts or noise,<sup>69</sup> thus improving the predictive performance of the calibration models. The pre-processed data of both CD and UV were partitioned into a calibration (80%) and a validation (20%) dataset using the Kennard-Stone algorithm,<sup>75</sup> which provides a representative split that gives an uniform distribution of samples.

Finally, the multivariate calibration models were built using partial least squares regression (PLS)<sup>71, 72</sup> to relate the spectra data to the compositions  $x_{S+R}$ ,  $x_{S-R}$  and  $x_{S-MA}$ . PLS is a multivariate regression method with a compression of spectral data beforehand to reduce the number of variables present.<sup>72, 76</sup> The compressed variables obtained in PLS are referred to as latent variables (LV). The models were validated internally and externally using cross-validation and the validation datasets to test their reliability and accuracy.<sup>63</sup> To minimize overfitting, the optimum latent variables (LV) were chosen with a maximum explained variance for cross-validation using a random subset approach with 30 data splits and 15 iterations.

To compare the model's predictions with experimental results from another quantification method, 28 compositions of different ratios in S and S-MA were analysed simultaneously by UV-CD spectroscopy and gravimetric method i.e. measuring solubility by mass difference between a solution and its solid obtained after complete evaporation.

## **2.5. Phase diagram construction: Equilibration technique**

The experimental compositions for equilibration were estimated at the chosen temperature of 9°C for phase diagram construction, based on existing data.<sup>36</sup> These compositions were prepared in 2 mL sealed vials. After dissolution at 50°C, they were cooled down to 9°C and seeded with stable solid phases in the corresponding system, to form stable suspensions. All vials were stored isothermally at  $9 \pm 1^\circ\text{C}$  under stirring, using Polar Bear Plus apparatus (Cambridge Reactor Design, UK) that enabled simultaneous equilibration of batches of 28 compositions. The compositions were left to equilibrate for 14 days after which the saturated solution and solid compositions were determined, which led to phase diagram points as summarized in Figure 4. The saturated liquid phases were sampled using a syringe with a filter. To obtain a final solution whose total component concentration is in the UV-CD calibration range for that system, a sample dilution ratio (i.e. the total mass of the dilution solvent divided by the mass of the saturated solution sample) from 10 to 300 was applied depending on the phase diagram region. Due to high dilution ratios, the liquid properties between saturated liquids and

diluted samples vary a lot. Therefore, weighing of saturated liquid and added solvent were mandatory for precision, as working with volumes proved to induce a significant error in data. The diluted solutions were then analysed by UV-CD spectroscopy. The obtained spectra were pre-processed and used as input into the model to determine the mass fractions  $x_R$ ,  $x_S$ ,  $x_{S-MA}$  and  $x_{MeCN}$  of each component in the diluted solution. The saturated liquid composition for each sample was then computed using the calculated sample dilution ratio and converted to molar fraction  $X$  to position the experimental point in the phase diagram. The solid phases in equilibrium with the saturated liquid were analysed by XRPD after filtration of the suspensions to conclude on the phase diagram region the point belongs to. Eutectic points and quaternary points, corresponding to solutions equilibrated with more than one solid, are identified by XRPD in which more than one solid phase is measured. When not measured experimentally, they are estimated at the intersection of extrapolated neighbouring solubility curves/surfaces.

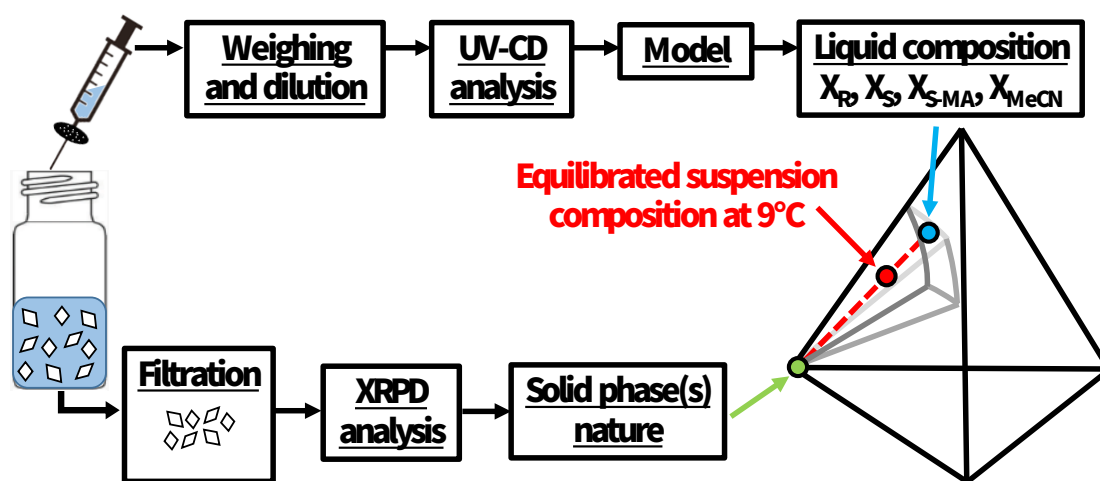


**Figure 4:** Protocol to obtain phase diagram composition from isothermal suspension at 9°C after 14 days.

### 3. Results

Using the UV-CD spectroscopy data from calibration samples, we develop multivariate PLS calibration models to compute multicomponent chiral compositions in unknown solutions. The validated models are applied to phase diagram determination in the R/S/S-MA/MeCN quaternary system represented as a tetrahedron plot in Figure 5. First, we detail the results regarding the spectral data and the calibration model specificities. Then, we present the revaluation of three solid-liquid ternary phase diagrams at 9°C, represented on the faces of the tetrahedron involving the solvent. We start with the phase diagram between R and S enantiomers forming a racemic compound RS (Figure 5a), then between S and S-MA forming a 1:1 enantiospecific cocrystal S:S-MA (Figure 5b), and next between R and S-MA forming no cocrystal (Figure 5c). Finally, the inside of the tetrahedron (Figure 5d) is investigated in detail for the first time as our models allow quantification of quaternary compositions, with the view to understand the solid phase stabilities and their solubilities as a function of component compositions.



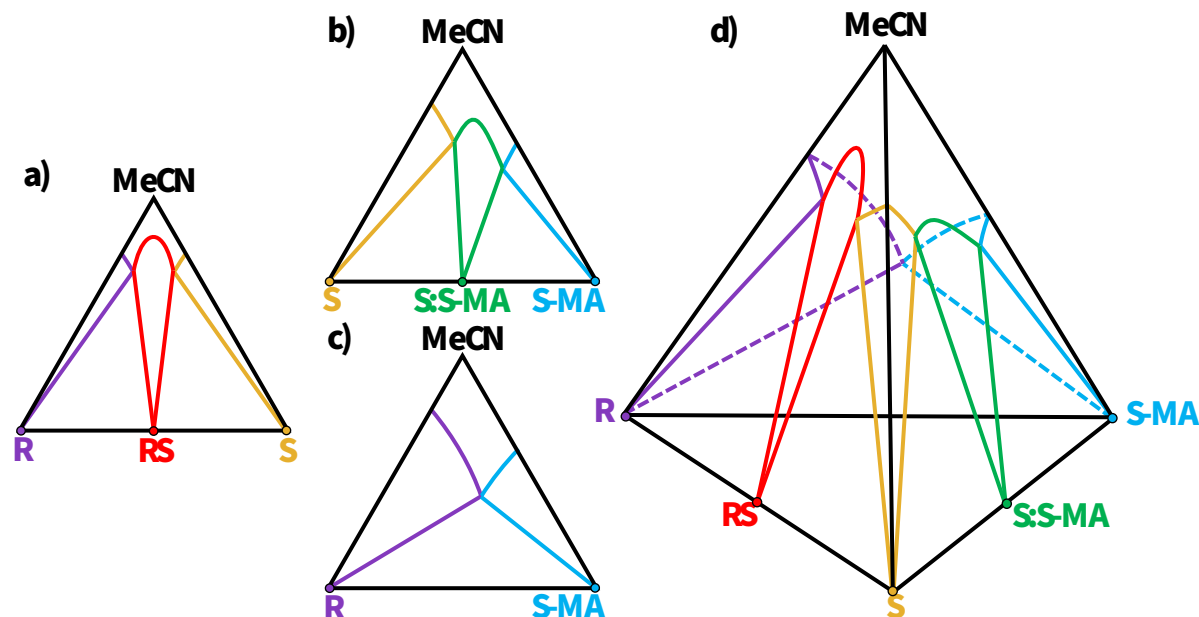


**Figure 5:** Isothermal and isobaric schematic phase diagrams of the four-component system: (R)- and (S)-2-(2-oxopyrrolidin-1-yl)butanamide (R and S), (S)-mandelic acid (S-MA) and the solvent acetonitrile (MeCN). The ternary phase diagrams were estimated in a previous study,<sup>36</sup> while solubility measurements inside the tetrahedron are tackled for the first time in the present study to understand phase stability and solubility variations in the quaternary diagram.

### 3.1. Multivariate PLS calibration models development from UV-CD spectra

#### 3.1.1. Spectral data in the quaternary system

To treat spectral data from UV and CD, defining a wavelength range where all dissolved molecules absorb UV is necessary. Since the solvent MeCN absorbs UV below 195 nm and R, S and S-MA do not absorb above 260 nm, the optimal wavelength range is chosen to be from 200 to 260 nm. The whole region is used for composition prediction using multivariate methods. In Figure 6a UV spectra for several calibration samples are represented. UV spectroscopy does not distinguish between the R and S enantiomers, and both molecules yield an absorption peak below the chosen wavelength range with a large part of the tail of this peak visible from 200 to 250 nm in Figure 6a (yellow solid line). S-MA shows similar UV absorption behaviour but additionally has a shoulder at 205 nm to 216 nm (Figure 6a, light blue solid line). Because of significant overlap in UV spectra of pure R/S and pure S-MA, the influence of each component in R/S and S-MA mixtures is difficult to distinguish but can be observed in the resulting spectra shape. Therefore, it assesses the necessity of using multivariate calibration for modelling, as it considers the effects of composition changes on the whole wavelength range at the same time. Both the normalized spectra shape for 50% S/50% S-MA (Figure 6a, green dashed line) and 33.3% of R, S and S-MA (Figure 6a, black dotted line) mixtures highlight this influence. The more S-MA a sample contains the more the inflexions are marked in the resulting spectra.

Figure 6b shows the CD spectra of the same calibration samples, where we observe that CD distinguishes both enantiomers. R and S give positive and negative symmetrical responses with peak

extrema at around 230 nm (purple and yellow solid lines). The 50%/50% mixture of R and S yields a flat line signifying the presence of equal amount of both enantiomers (red dashed line). S-MA has a positive CD spectrum with a peak at 223 nm (Figure 6b, light blue solid line). Significant overlap can be seen between the mixtures of R, S and S-MA, leading to different spectral shapes based on the component ratio. For instance, an equimolar ratio between R, S and S-MA results in a CD spectrum of the same shape as pure S-MA with a peak at 223 nm but with the intensity being a third, for the same total concentration (black dotted line). Therefore, despite the overlap, the shapes and intensities of the CD spectra show information on both the concentration difference between R and S and the S-MA concentration.

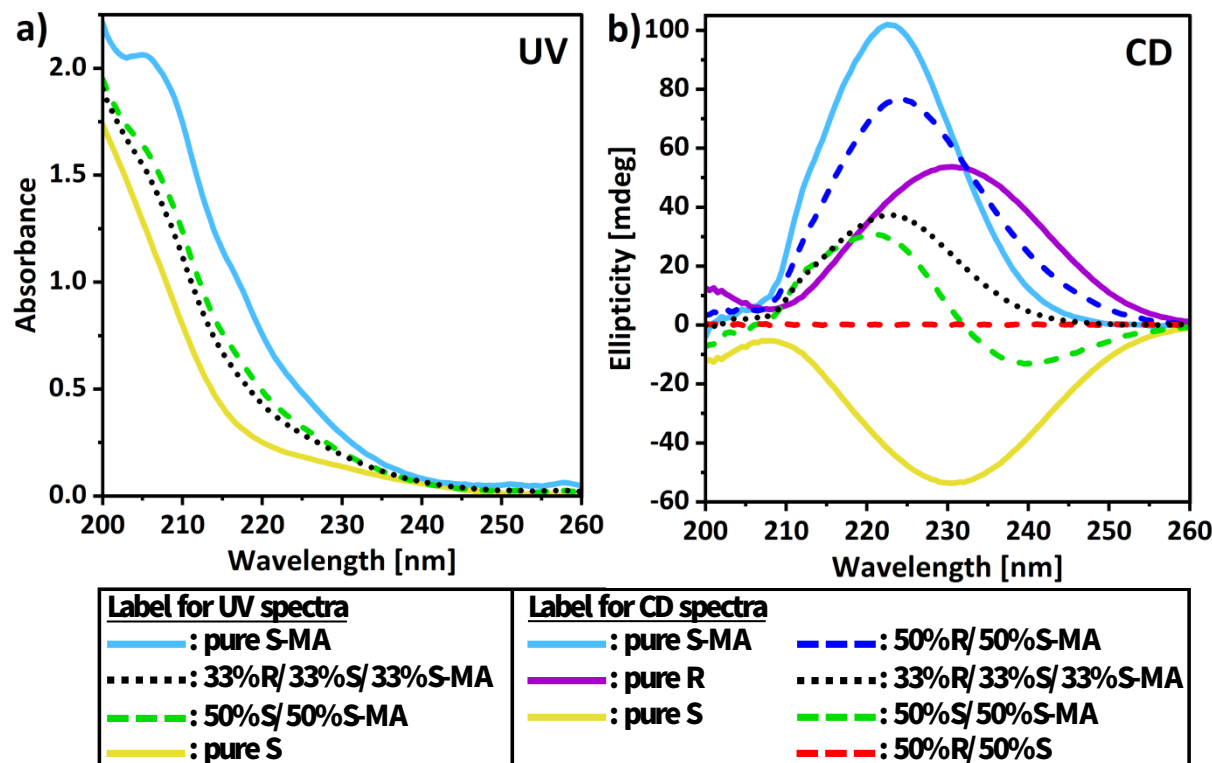


**Figure 6:** a) UV and b) CD spectra of solutions with a normalized total concentration of 4 mg/mL: pure components (solid lines), binary mixtures (dashed lines), ternary mixtures (dotted lines).

### 3.1.2. Multivariate PLS calibration models specificities

The results of PLS calibration models for the quantitative prediction of  $x_{S+R}$ ,  $x_{S-R}$  and  $x_{S-MA}$  are summarised in Table 1. Their reliabilities and accuracies were evaluated internally and externally using cross-validation and the validation datasets. The root mean square error of prediction (RMSEP) is computed to estimate the error in predicting the measured values of a known sample, while the root mean square error of cross validation (RMSECV) estimates the error in predicting the values of a calibration sample. The models are also tested by  $R^2$  (goodness of fit) and  $Q^2$  (goodness of prediction) values.  $R^2$  gives the amount of variance explained by the model and the  $Q^2$  gives the amount of variance predicted by the model. Both PLS models required only two latent variables (LV)

to compress the spectral data variables and capture the variance in the data, while giving good predictions with high linearity ( $R^2 > 0.99$ ,  $Q^2 > 0.97$ ). The high accuracy is highlighted by the levels of RMSEP and RMSECV that show a lower order of magnitude for mass fraction errors than the mass fraction values of the calibration samples (see Supplementary Information Table S1).

**Table 1:** Results of PLS calibration models for UV and CD spectral data acquired in the 200 to 260 nm range describing the accuracy in the composition prediction. The results are the number of latent variables (LVs) required, the root mean square error of prediction (RMSEP), the root mean square error of cross validation (RMSECV), the goodness of fit  $R^2$ , and the goodness of prediction  $Q^2$ .

Data	Method	Value predicted	N° of LVs	RMSEP ( $\times 10^{-6}$ ) (g/g)	RMSECV ( $\times 10^{-6}$ ) (g/g)	$R^2$	$Q^2$
UV	PLS	$x_{S+R}$	2	16.3	13.0	0.997	0.977
		$x_{S-MA}$		14.5	12.0		
CD	PLS	$x_{S-R}$	2	12.0	1.16	0.998	0.986
		$x_{S-MA}$		15.4	11.1		

Figure 7 shows the predicted values of calibration samples through the calibration models versus their actual values for  $x_{S+R}$  (a),  $x_{S-R}$  (b) and  $x_{S-MA}$  (c, d), to visualise the goodness of fit. It can be observed that the split of samples between validation sets (green triangles) and calibration sets (blue points), performed using the Kennard-Stone algorithm,<sup>75</sup> is uniform in the distribution and therefore representative. The values of  $x_{S-R}$  from CD in Figure 7b range from positive to negative, representing an excess of S and R in the sample, respectively. Very strong linearity along the diagonal lines in red can be seen in the plots for all samples, meaning prediction is very close to the actual value. The linearity relates to RMSEP and RMSECV values that quantify the error on how much samples from the calibration sets and validation sets deviate from the diagonal line, therefore giving an estimation of the average error in a prediction. There is no significant difference between  $x_{S-MA}$  predicted from both the UV and CD measurements (Figure 7c and Figure 7d), with RMSEP and RMSECV values being very similar, thus showing the accuracy and consistency of the models. However, the PLS model with CD data gives the best prediction with the lowest RMSECV and  $R^2$ . Therefore, the  $x_{S-MA}$  value from CD is always used in calculations for accuracy.

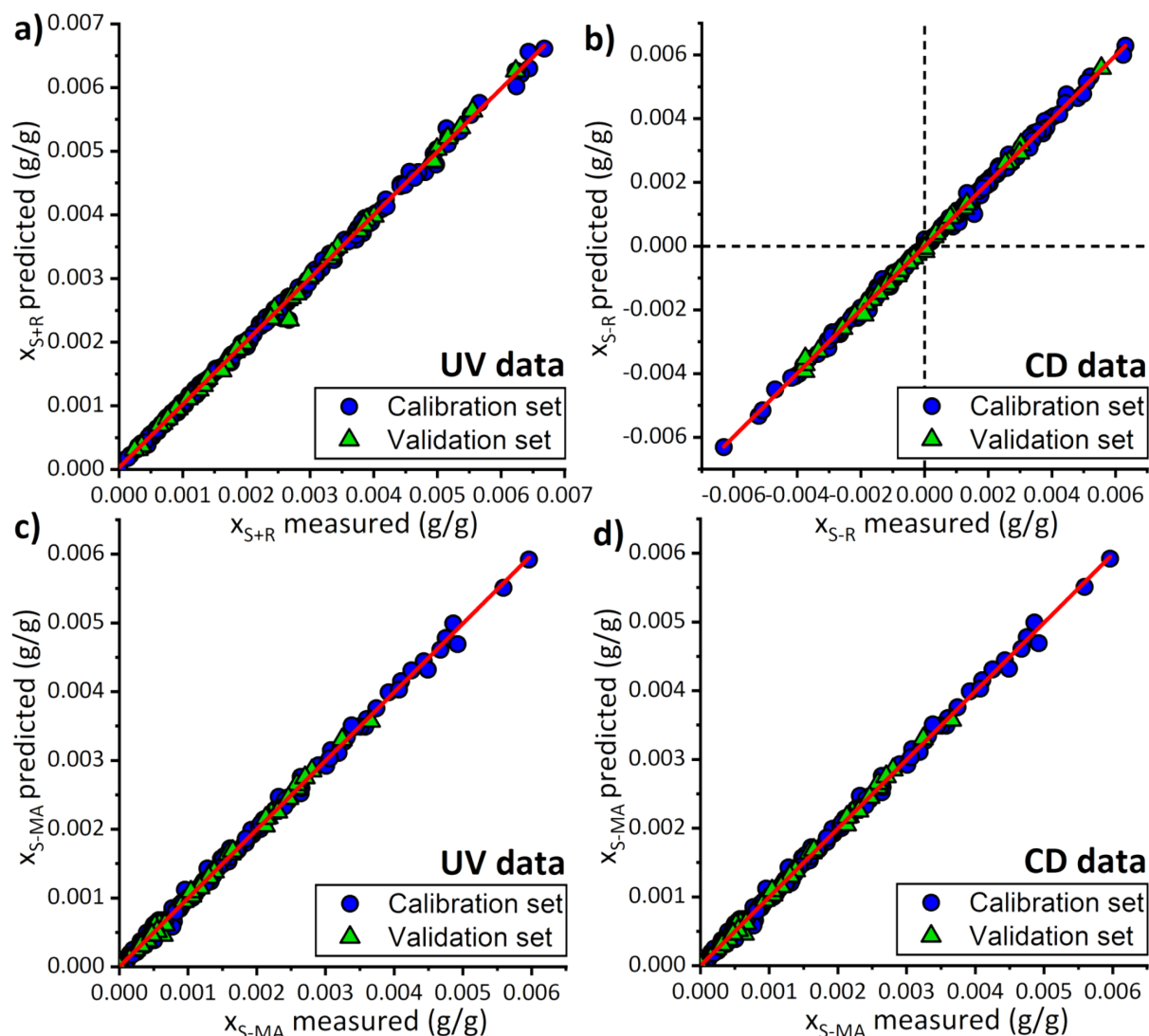


**Figure 7:** Plots for experimental values of calibration samples versus their predicted values through the calibration models for **a)** Total mass fraction in enantiomers  $x_{S+R}$  (UV data) **b)** Differential enantiomers mass fraction enantiomers  $x_{S-R}$  (CD data) **c)** Mass fraction in S-MA  $x_{S-MA}$  (UV data) **d)** Mass fraction in S-MA  $x_{S-MA}$  (CD data).

The UV-CD model predictions are compared with results obtained from the gravimetric method for 28 compositions of different ratios in S and S-MA that were analysed simultaneously by UV-CD spectroscopy. The percentage error  $\delta$  (%) =  $\frac{|X - Y|}{Y}$  is used for comparison, with X being the total solubility obtained with the UV-CD model result, and Y the total solubility from the gravimetric method, on the same saturated solution. It shows a mean  $\delta$  of 2.09% between the two methods on the total solubility, with a standard deviation of 1.47% (see Supplementary Information Table S2). Even though gravimetry is not an accurate quantification method, particularly when using a single measure, it relies on a physical measurement and therefore confirms that our multivariate calibration models do not have a bias in their calculations. These validated calibration models allow accurate

determination of the mass fractions of unknown solutions in R ( $x_R$ ), S ( $x_S$ ), S-MA ( $x_{S-MA}$ ) and MeCN ( $x_{MeCN}$ ), and therefore they are used for computing the phase diagram data.

### **3.2. Isothermal ternary phase diagrams**

#### **3.2.1. Ternary system of R/S/MeCN**

In the R/S/MeCN system, the stable solids consisting of pure R, pure S and pure racemic compound RS are expected to crystallize at equilibrium. 26 equilibrated solution compositions, with enantiomeric excess ( $E$ ) values from 0% to 100%, are computed from experimental results. Due to symmetry along racemic compositions in enantiomeric systems, 26 additional points corresponding to negative values of enantiomeric excess ( $E$ ) are deduced from the mirror projection of the first 26 points. The isothermal ternary phase diagram of R and S in MeCN at 9°C is plotted in Figure 8. Solubility lines correspond to the typical shape of a stable racemic compound in an isothermal ternary system and solid phases in equilibrium are confirmed. This phase diagram is in excellent agreement with previous data obtained with a combination of achiral and chiral chromatography methods (Figure 8, beige diamonds).<sup>36</sup>

The eutectic points  $a$  and  $b$  (Figure 8, grey triangles) are obtained with an experimental composition presenting S and RS in stable suspension. These points fit perfectly with the intersection of neighbouring solubility curves. Experimental solubility values of pure R, S and RS solids, with compositions of eutectic points  $a$  and  $b$ , are compiled in Supplementary Information Table S3. All data point compositions with related solid phases identified at equilibrium used in Figure 8 are given in the Supplementary Information Table S4. Only the pure enantiomer solubility differs slightly from previous data.<sup>36</sup> However, we note that our value is confirmed through the repetition of four measurements in different saturated solutions of pure S, with UV-CD and the gravimetric method used to compare the model's prediction. Both methods lead to the same value with about 0.5 mg/mL variation (see Supplementary Information Table S5).

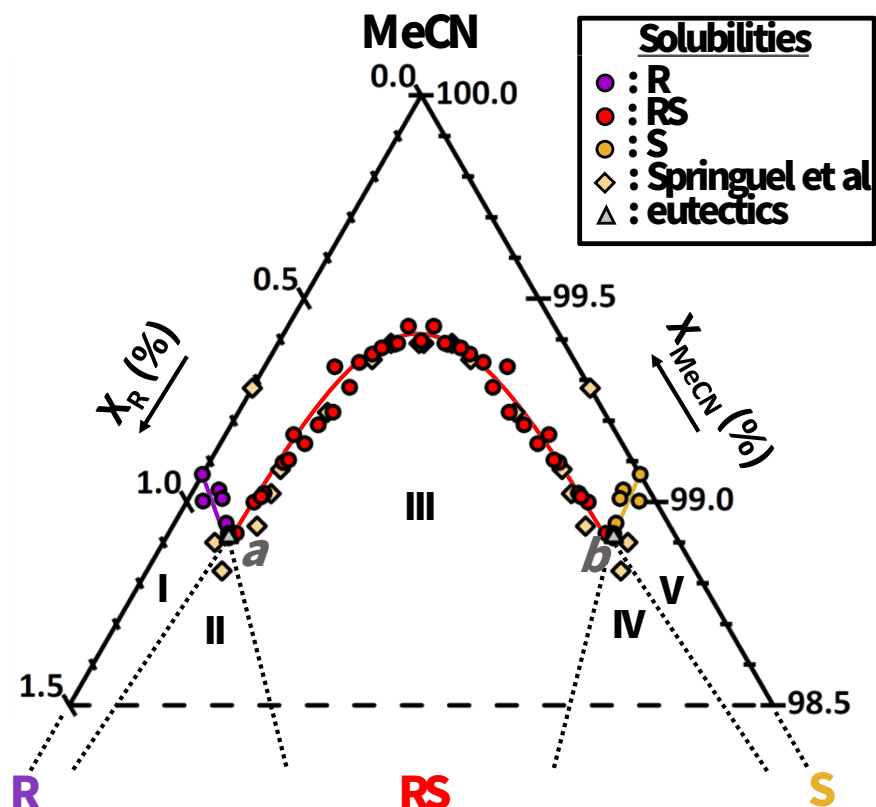


**Figure 8:** The isothermal ternary phase diagram of R and S in MeCN at 9°C showing a racemic compound system. Regions I, III and V are respectively the stability domains in which an overall composition phase splits into a saturated solution and respectively the solid R (purple solubility points), racemic solid RS (red solubility points) and the solid S (yellow solubility points). Regions II and IV are triphasic domains between the racemic compound RS, a solution of eutectic composition (grey triangle) and R and S, respectively. Above the solubility lines is the single-phase domain of the undersaturated solution. Dotted lines are boundaries between stability domains. Beige diamonds are the solubility points from the Springuel et al. study obtained with achiral and chiral chromatography.<sup>36</sup> Note that the phase diagram is zoomed in to the solvent corner. Data points used for the construction of this diagram are detailed in the Supplementary Information (Table S4). Eutectic points *a* and *b* were measured experimentally with a composition presenting S and RS in stable suspension.

No significant solubility modification effect is observed for pure R (purple) and pure S (yellow) solid solubility points due to the presence of the other component as  $X_R$  and  $X_S$  stay relatively constant. The solubility increase for  $X_R$  and  $X_S$  values at the eutectic points *a* and *b* is only 2%. Where the racemic compound RS equilibrates (red points), its solubility  $(X_R.X_S)^*$  shows an important curvature depicting lower  $X_R$  values than  $X_R$  at the eutectic *a*, down to a minimal total solubility  $(X_R + X_S) = 0.6 \%$  for pure RS at 1:1 stoichiometry between R and S. The solubility of the pure enantiomer in the pure solution is 1.5 times higher than pure RS total solubility in a racemic solution. Maximum total solubilities are reached in eutectic points where the total solubility is 1.2 times higher than pure R and S and 1.8 times higher than pure RS solubility.

### 3.2.2. Ternary system between S/S-MA/MeCN

In the S/S-MA/MeCN system, the stable solids consisting of pure S, pure S-MA and pure 1:1 enantiospecific cocrystal S:S-MA are expected to crystallize at equilibrium. Experimental solubilities are computed from experimental results of 55 equilibrated suspensions of varying ratios between S and S-MA in MeCN. The isothermal ternary phase diagram at 9°C is plotted in Figure 9, zoomed in to the solvent corner. The phase diagram corresponds to a stable 1:1 cocrystal forming system between S and S-MA. As the theoretical line between the 1:1 stoichiometry of the S:S-MA solid phase and the pure solvent MeCN crosses the solubility curve of S:S-MA (green), the cocrystal exhibits a congruent solubility at 9°C, meaning it forms a stable suspension in solutions with the same stoichiometry as the cocrystal.

The eutectic point *c* is obtained at an experimental composition presenting S and S:S-MA in stable suspension. It fits well with the intersection of neighbouring solubility curves. The eutectic point *d* is estimated at the intersection of converging solubility curves. In Figure 9, the phase diagram solubility points and domain shapes differ slightly from previous data and their interpretation with fewer data points on the same system by Springuel et al.,<sup>36</sup> as they suggested the cocrystal to have an incongruent solubility (diamond points). Here, with more data points presented, and an experiment resulting in eutectic solution composition *c* with S and S-MA solids in suspension, we reevaluate the stability domains. A shift can also be observed between some of their solubility data and ours, even in pure component solubilities. We checked the latter through the repetition of four measurements in different saturated solutions of pure S and pure S-MA with UV-CD model and the gravimetric method that was used when validating the model's predictions by comparison with an external method. It gives consistent values and negligible variations (see Supplementary Information Table S5). Moreover, 28 saturated solutions from our ternary system were validated simultaneously by the gravimetric method (see Supplementary Information Table S2). Therefore, we propose an accurate reevaluation of the phase diagram using consistent results. Experimental solubility values of pure S, S-MA and S:S-MA solids, with compositions of eutectic points *c* and *d*, are compiled in Supplementary Information Table S3. All data point compositions with related solid phases identified at equilibrium used in Figure 9 are given in the Supplementary Information Table S6.

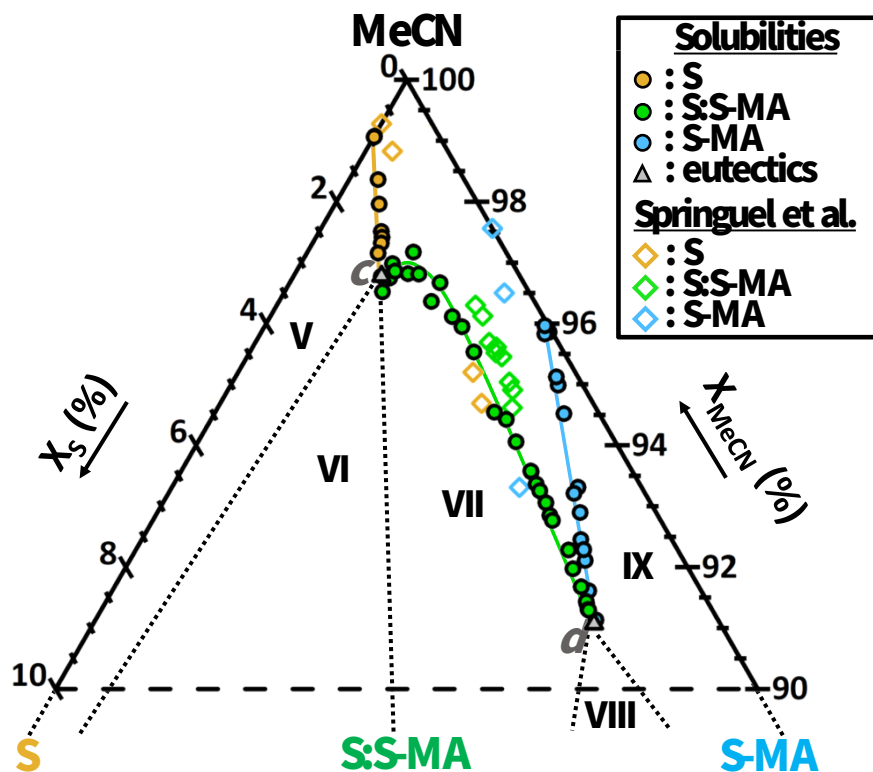


**Figure 9:** The isothermal ternary phase diagram of S and S-MA in MeCN at 9°C showing an enantiospecific cocrystal system. Regions V, VII and IX are the stability domains in which an overall composition phase splits into a saturated solution and the solid S (yellow solubility points), the cocrystal S:S-MA (green solubility points) and the solid S-MA (blue solubility points), respectively. Regions VI and VIII are triphasic domains between the cocrystal S:S-MA, a solution of eutectic composition (grey triangle) and S and S-MA, respectively. Above the solubility lines is the single-phase domain of the undersaturated solution. Dotted lines are boundaries between stability domains. Diamonds are the solubility points from Springuel et al. study obtained with achiral and chiral chromatography.<sup>36</sup> Note that the phase diagram is zoomed in to the solvent corner. Data points used for the construction of this diagram are detailed in the Supplementary Information (Table S6). Eutectic point c was measured experimentally in a composition presenting S and S:S-MA in stable suspension. Eutectic point d was estimated at the intersection of converging solubility curves.

A strong effect on the solubility of pure S solid is observed (yellow) as a function of the concentration of S-MA: the solubility  $X_S$  at the eutectic point c is 2.1 times higher than that in the pure solvent. The total solubility at eutectic point c, including the S-MA concentration, is 3.5 times higher than that in the pure solvent. Similarly, pure S-MA solid solubility points (blue) are increased by the presence of S, up to a solubility  $X_{S-MA}$  at eutectic point d that is 1.8 times higher than for pure S-MA solubility, while the total solubility is 2.2 times higher than for S-MA in the pure solvent. The solubility  $(X_S \cdot X_{S-MA})^*$  of the S:S-MA cocrystal (green points) decreases as a function of concentration of S and S-MA, from a maximum value at the eutectics, down to a minimum solubility point that is the pure S:S-MA congruent solubility value at 1:1 stoichiometry between S and S-MA, for a minimal total solubility  $(X_S + X_{S-MA}) = 3.2\%$ . The solubility of S-MA in pure solvent is 1.3 times higher than the total solubility of S:S-MA, whose  $X_{S-MA}$  is divided by 2.5 compared to the pure S-MA solubility. However, the total solubility of pure S:S-MA is 3.4 times higher than pure S, with  $X_S$  being 1.7 times the pure S solubility.



The possible explanations for the increase in solubility of pure S and pure S-MA solids with the presence of the other component in solution, are most likely due to favourable intermolecular interactions between components in solution. Nevertheless, solution complexation is also a possible reason as it has been reported to occur for some cocrystal components.<sup>77</sup>

### **3.2.3. Ternary system between R/S-MA/MeCN**

In the R/S-MA/MeCN system, the stable solids consisting of pure R and pure S-MA are expected to crystallize at equilibrium. Experimental solubilities are computed from experimental results of 28 equilibrated suspensions of varying ratios between R and S-MA in MeCN. The isothermal ternary phase diagram at 9°C is plotted in Figure 10, zoomed in to the solvent corner. Contrary to the S/S-MA/MeCN system, no cocrystal forms between R and S-MA as the solubility lines seem to converge to a single eutectic point *e* and no new solid phase is identified in the experiments. Therefore, it confirms the enantiospecific nature of the S:S-MA cocrystal identified from the Springuel et al. study.<sup>31</sup>

Solubility lines show a strong influence of the components on each other's solubility, with the total solubility increasing sharply in mixtures. The solubility of R is increased more by the concentration of S-MA than the solubility of S in the S/S-MA/MeCN system. This strong increase of the solubility of R with the S-MA concentration, coupled with the absence of cocrystal formation, is causing the eutectic point *e* to be a deep eutectic. This strong affinity between components was already reported in the binary system of R and S-MA,<sup>31</sup> whose binary eutectic temperature of around 32°C is about 100°C deeper than the pure R and pure S-MA melting points. Therefore, in the R/S-MA/MeCN ternary system at 9°C, it induces a small triphasic domain between R, S-MA and a saturated liquid of eutectic composition *e* that is at a very high equilibrium concentration. This leads experimentally to a big increase in sample viscosity as solubility increases strongly for compositions close to the eutectic point *e*, making it difficult to estimate as the solutions are too viscous to be accurately sampled for liquid analysis. Trial experiments to screen eutectic point *e* are represented in Figure 10 by square points, that correspond to five highly concentrated suspensions left at 9°C for more than three weeks, after complete dissolution and seeding with a small amount of R and S-MA solids. For three compositions (blue squares), a very small amount of solid phase crystallizes in the highly viscous liquids. The isolated solid, characterised using XRPD, is pure S-MA despite a low intensity signal because of the small amount of solid recovered. For the two other compositions (white squares), the liquor remains clear with no crystallization happening, it is then assumed they belong to the undersaturated solution domain. These results help to estimate roughly the extension of solubility lines and to define a compositional region in which the eutectic point *e* is positioned. For the system representation and description purposes, the composition of eutectic point *e* is an approximation. Experimental solubility values of pure R, S-MA and estimation of eutectic point *e* are compiled in Supplementary Information Table S3. All data point compositions with related solid phases identified at equilibrium used in Figure 10 are given in the Supplementary Information Table S7.

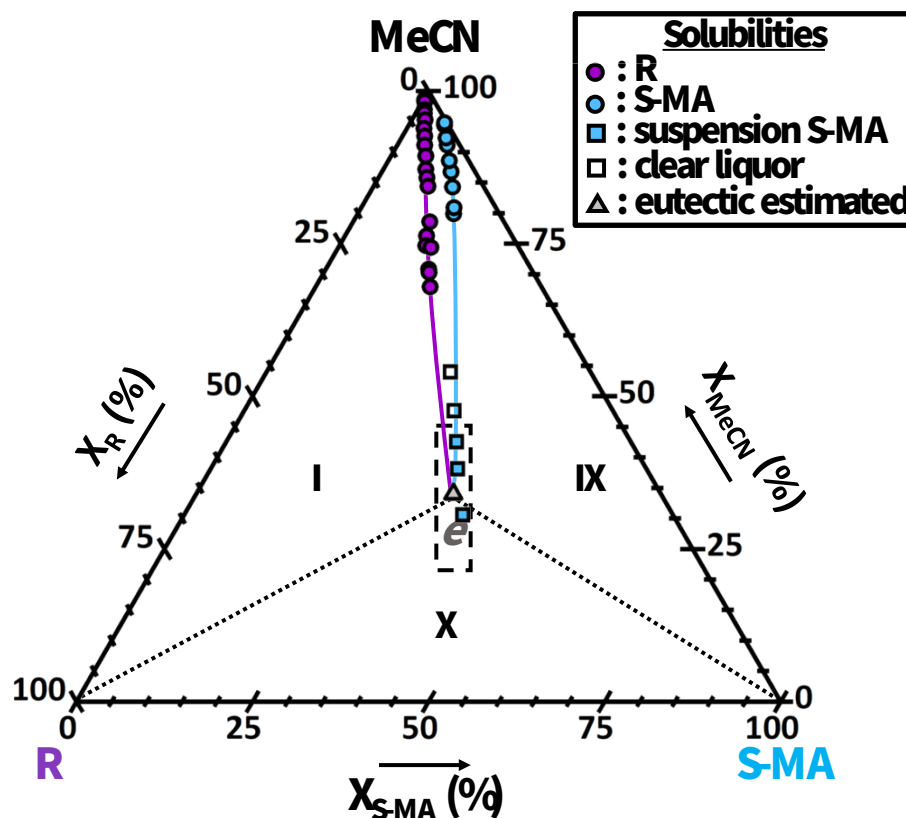


**Figure 10:** The isothermal ternary phase diagram of R and S-MA in MeCN at 9°C showing a single eutectic equilibrium. Regions I and IX are the stability domains in which an overall composition phase splits into a saturated solution and the solids R (purple solubility points) and S-MA (blue solubility points), respectively. Region X is the triphasic domain between R, S-MA and a solution of eutectic composition *e* (grey triangle). Above the solubility lines is the single-phase domain of the undersaturated solution. Dotted lines are boundaries between stability domains. Blue squares correspond to overall compositions of which, due to the high viscosity, only the equilibrated solid could be sampled for XRPD analysis to be identified as S-MA. White squares correspond to sample compositions in which no solid was present after the equilibration period. The dashed box is the region in which eutectic point *e* is estimated, from extrapolation of solubility curves and suspensions obtained at blue squares. The centre of the box is chosen as the most likely estimation. Data points used for the construction of this diagram are detailed in Supplementary Information (Table S7).

An important solubility increase effect is observed for the pure R solid solubility points (purple) as  $X_R$  values increase due to the increasing presence of S-MA, up to an estimated value of about 32 times higher than pure R solubility at the estimated eutectic point *e*. The total solubility at eutectic point *e* is about 70.7 times higher than for pure R in MeCN. Similarly, pure S-MA solid solubility points (blue) are increased by the presence of R, up to a  $X_{S-MA}$  value being about 9 times higher than pure S-MA solubility at eutectic point *e*, whose total solubility is about 16 times higher than for pure S-MA in MeCN. The solubility behaviour of the R/S-MA/MeCN system is therefore very different from that of the S/S-MA/MeCN system, with a stronger impact of R solubility with S-MA concentration than it is for S solubility, and no cocrystal forming. This difference will cause a huge asymmetry in the quaternary system. Favourable intermolecular interactions between

components in solution could be the reasons why the solubility of pure R and pure S-MA solids increase with the presence of the other component in solution. Another possibility is the occurrence of solution complexation between the components.<sup>77</sup>

### 3.3. Quaternary system with R/S/S-MA in MeCN at 9°C

After investigating the three isothermal ternary phase diagrams that correspond to each face of the quaternary tetrahedron, the full isothermal quaternary phase diagram has been explored using 168 equilibrated quaternary suspensions distributed inside the tetrahedron. In this system, all stable solids from the ternary systems, consisting of pure R, S, S-MA, RS and S:S-MA are expected to crystallize at equilibrium. As for every phase diagram, quaternary phase diagrams follow the Gibbs phase rule<sup>78</sup> which defines the number of degrees of freedom,  $\nu$ , that are independent intensive parameters required to define an equilibrium state. The Gibbs phase rule is expressed as

$$\nu = C + N - \phi \quad \text{Gibbs phase rule equation}$$

where  $C$  is the number of independent components (in this case  $C=4$ ),  $N$  is the number of intensive parameters that the system depends on (in this case  $N=0$ ) and  $\phi$  is the number of phases in equilibrium, giving  $\nu = 4 - \phi$  for this system.

The maximum total solubility point in this quaternary phase diagram is measured to be about 140 times higher than the minimal total solubility point, making it impossible to clearly represent the full characteristics of the quaternary in the 3D phase diagram. Therefore, a solvent-free projection of solubility surfaces is used in Figure 11 (left) to display all experimental points from the quaternary system and related ternary systems. By removing the dependency on the solvent concentration, solubility data can be shown in a two-dimensional plot where points are positioned based on their relative solvent-free molar ratio in dissolved components (R, S, S-MA). Explanations about how solvent-free projections are performed from phase diagram solubility points are provided in Supplementary Information (Figure S3). The points in Figure 11 (left), are coloured according to the solid phase(s) identified in equilibrium for each saturated solution. The points identified as belonging to biphasic domains ( $\nu = 2$ ) correspond to a split of an overall composition between a saturated solution and one of the solids R (purple), S (yellow), S-MA (blue), RS (red) or S:S-MA (green). When two solids are identified at equilibrium (light grey), the points belong to a triphasic domain ( $\nu = 1$ ) of which the measured saturated solution is a eutectic composition, similarly to previously measured eutectics in ternary sections (light grey triangles). A maximum of three solids can be identified as stable in a suspension at equilibrium (dark grey squares), that is therefore part of a quadriphasic domain ( $\nu = 0$ ) of which the measured saturated solution is the unique possible liquid composition, referred here as a quaternary point.

Figure 11 (right) is our interpretation of experimental points in the solvent-free projection. Biphasic domains points cover a region defining a solubility surface, whose colour is chosen depending on the related stable solid. These regions have boundaries that are a part of the figure sides corresponding to the solid solubilities in the ternary phase diagrams (black lines) down to a ternary eutectic point (light grey triangle). For example, the solubility surface of pure S (yellow) presents the solubility data from R/S/MeCN and S/S-MA/MeCN ternaries, from pure S solubility to

ternary eutectic points *b* and *c*. The boundaries between regions are also eutectic lines (dark grey) that link eutectic compositions associated to triphasic domains that equilibrate the two same solids, each being from the neighbouring solubility surfaces. The eutectic lines can link a ternary eutectic point with a quaternary point that presents the two same solids at equilibrium. For instance, between ternary eutectic *b* showing *S* and *RS* solids equilibrating in the liquid, and quaternary point *f* equilibrating *S*, *RS* and *S:S-MA* in suspension. It can also link two quaternary points presenting the same two solids in their equilibrated suspensions, such as quaternary points *f* and *h* both equilibrating *RS* and *S:S-MA* among their stable solids. Quaternary points always correspond to the intersection of three eutectic lines, as they represent the solution of unique composition possible in a quadriphasic domain ( $v = 0$ ), saturated in the three stable solids in suspension, according to the Gibbs phase rule.<sup>78</sup> For example, the quaternary point *f* is the saturated solution corresponding to *RS*, *S* and *S:S-MA* in stable suspension. It is identified experimentally with a XRPD result presenting the three solids signatures. We can observe it fits perfectly with the convergence of three eutectic lines equilibrating two of these solids.

The arrows shown in Figure 11 (right) are pointing towards the direction of increasing total solubility, to represent the relative quantity of solvent in the saturated solutions based on experiments results. The pure solid phases are always presenting a total solubility lower than the ternary eutectic points they are linked to, therefore with an arrow pointing down to them. The ternary eutectic points themselves have a lower total solubility than the quaternary point they are linked to, and consequently an arrow directed towards them. For instance, the total solubility of quaternary point *f* is 3.7 times higher than ternary eutectic point *b* and 1.3 times higher than ternary eutectic point *c*. Its solubility in *S* is the highest of the whole stability domain of *S*, being 2.3 times higher than pure *S* solubility. Between, two quaternary points linked, there is no rule regarding the direction of evolution of total solubility. Overall, *S/S-MA/MeCN* ternary system (*S* to *S-MA* axis) exhibits a much lower solubility than the *R/S-MA/MeCN* one (*R* to *S-MA* axis). Figure 11 (right) reflects this huge difference by a substantial asymmetry in the quaternary system. All solubility surfaces dive towards compositions close to the estimated eutectic point *e*, as shown in the direction of the eutectic lines. The lack of experimental data in Figure 11 close to eutectic point *e* is again due to viscous solutions, difficult to equilibrate and sample. Four eutectic lines are converging in this region but the way they meet cannot be determined precisely. However, because of the Gibbs phase rule,<sup>78</sup> it is impossible for four phases to be in equilibrium with one composition in such isothermal isobaric quaternary system. Therefore, there must exist the two quaternary points, *g* and *h*, each being the intersection of three eutectic lines. The compositional zones in which they are expected can be estimated from the extension of the eutectic lines, as represented in Figure 11, to compute an approximate solvent-free ratio (see Supplementary Information Table S3). We also know that both total solubilities at *g* and *h* are higher than at eutectic point *e*, that we estimate to be approximately 6g/mL MeCN. However, it is not possible to know whether *g* or *h* has the highest overall solubility, and, therefore, the direction of the eutectic line in-between is unknown. Experimental solubility values of all pure solid phases, ternary eutectic points and quaternary points are compiled in Supplementary Information (Table S3). Compositions of all saturated solution points in the quaternary phase diagram can be found in Supplementary Information (Table S8).

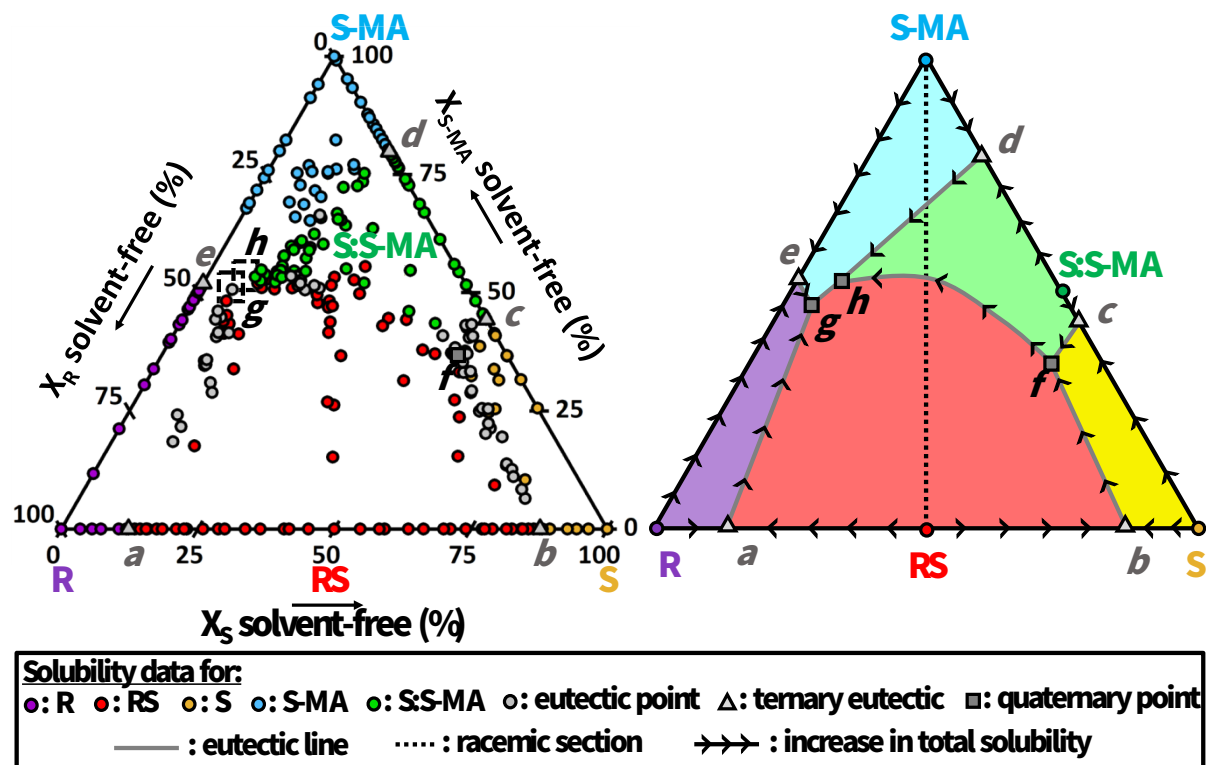


**Figure 11:** Left: projection of experimental results from the equilibration experiments showing the solvent-free solution compositions in the quaternary phase diagram R/S/S-MA/MeCN at 9°C. The colours of the points indicate the solids that are equilibrated with a saturated solution. Dashed boxes are compositional zones in which quaternary points are not measured but expected. All data used in the quaternary phase diagram can be found in Supplementary Information (Table S8) Right: interpretation of results projection into solubility surfaces, eutectic lines, and quaternary points. Arrows point towards the direction of increasing total solubility. The dotted black line represents the racemic section in the quaternary (equimolar ratio between R and S).

Figure 12 shows a schematic interpretation of the full quaternary phase diagram as a tetrahedron plot, based on experimental data points plotted in Supplementary Information (Figures S4 and S5) for different scales and viewing angles in the tetrahedron. Figure 12 is therefore not a representation to scale, because of the large variation in total solubility in the full tetrahedron. We can identify the shapes and boundaries of the five biphasic stability domains, highlighting every possible composition that leads to the stable suspension of a pure stable solid (R, S, RS, S-MA, and S:S-MA) in a saturated solution through tie-lines. All possible saturated solutions spread as a solubility surface at the separation with the undersaturated solution domain whose apex is pure MeCN. Eutectic lines are identified on the intercept of two solubility surfaces and define a line of saturated liquids in both neighbouring solid phases stability domains. The triphasic domains, not highlighted here for clarity, correspond to the zone of existence of suspensions following this equilibrium, linking saturated liquids from the eutectic lines to the two pure solids through tie-triangles. At the intersection of three eutectic lines are the quaternary points, of unique liquid composition possible for suspension of three solids. The quadriphasic domain, not highlighted here for clarity, is a tetrahedron zone whose apexes are the three pure solids and the quaternary point, defining the

existence zone of the suspensions. Inside, the phase compositions are not changing, only the mass balance between them is varying.

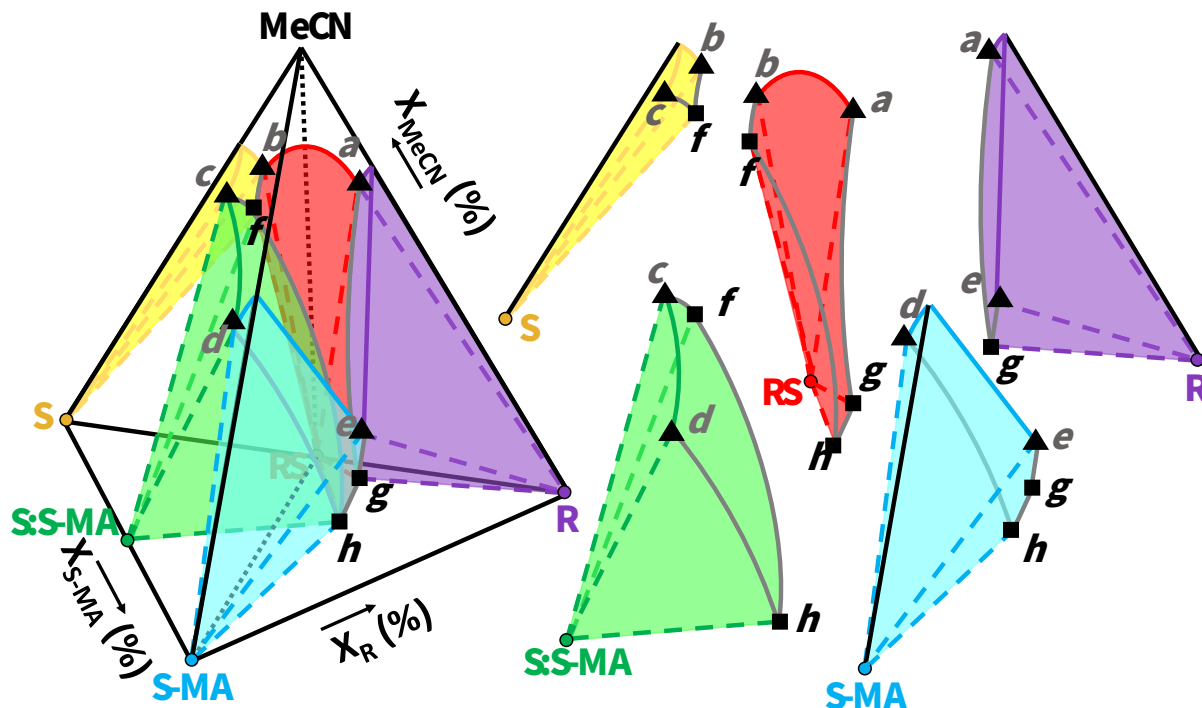


**Figure 12:** Graphical interpretation, not to scale, of the R/S/S-MA/MeCN quaternary phase diagram and the expanded view of biphasic stability domains of pure solid phases with their related coloured solubility surface in equilibrium. Black triangles correspond to eutectic points in the ternary systems, and grey lines to eutectic lines originating from them, representing the equilibrium liquid composition lines saturated in two solid phases from adjacent domains. At the intersection of three eutectic lines are quaternary points (black squares) corresponding to the liquid composition saturated in the three neighbouring solid phase domains. For clarity, the figure does not highlight triphasic domains (domain of tie-triangles linking eutectic lines to the two solids they are saturated in) and quadriphasic domains (domain whose boundaries are quaternary points linked with their three solids in equilibrium). The black dotted line indicates a cross-section of racemic composition (composition equal in R and S) in the quaternary.

## 4. Discussion

In pure racemic compound systems, such as the ternary system R/S/MeCN, it is impossible to perform crystallization-enhanced chiral separation under stable conditions by starting from a racemic solution. Therefore, crystallization-enhanced chiral resolutions are performed using kinetic processes like preferential crystallization. As stable racemic compound systems occur in 90 to 95% of cases for crystallization equilibria of chiral molecules, it makes chiral resolution complex. Nonetheless, the symmetry in enantiomeric systems can be broken when adding a chiral component such as S-MA, that can form enantiospecific solids such as the S:S-MA cocrystal, even in racemic solutions. By determining the R/S/S-MA/MeCN quaternary phase diagram, we show the boundaries and shapes of the stability domains of all stable solids in the system. This leads to the understanding of the relation between overall composition and solid formation. We observe a huge asymmetry in the S/S-MA/MeCN ternary system, forming a stable S:S-MA cocrystal of low solubility, and the R/S-MA/MeCN

ternary system highlighting a strong affinity between components in solutions, therefore reaching very highly concentrated solubility points. The consequence for the quaternary system is that the stability domain of S:S-MA is strongly skewed towards the opposite face of the tetrahedron, and therefore extends beyond the racemic composition. Indeed, in both Figure 11 and Figure 12, we can observe that the racemic composition (Figure 11, dotted line) crosses the solubility domains of RS (red), S:S-MA (green) and S-MA (blue). This asymmetry highlights a zone along the racemic cross-section RS/S-MA/MeCN where the S:S-MA cocrystal is accessible for crystallization. A chiral resolution experiment in this zone has the advantage of being in stable conditions as the phase diagram describes thermodynamic equilibrium, with S:S-MA being the only solid present at equilibrium. This was experimentally proved by Springuel et al.<sup>31</sup> To optimize chiral resolution in this zone, the knowledge of the entire quaternary phase diagram is required to define accurately the best working compositions. Based on the quaternary phase diagram data acquired here, it is possible to design process conditions during which the racemic compound RS and the chiral coformer S-MA as input can lead to obtaining only S:S-MA chiral cocrystal as output. Afterwards, the cocrystal can be separated into its pure components and thereby the pure levetiracetam API (S), a nootropic drug used as an anticonvulsant to treat epilepsy. Therefore, the knowledge of complex phase diagrams can help in designing alternative chiral separation routes with crystallization for industry.

The need for complex chiral phase diagrams is limited due to the difficulty in quantifying chiral molecules in multicomponent chiral systems. With UV-CD spectroscopy and multivariate calibration models, we have managed to quantify different chiral molecules in solution with great accuracy and are not limited by the increasing number of chiral components. This enlarges the range of methods available for chiral molecule quantification, used here for phase diagram determination, and especially on multicomponent systems such as quaternary systems that were difficult to access until now. The UV-CD spectroscopy method can be extended to even more complex systems, if necessary, with appropriate multivariate calibration models. As multivariate techniques consider the variations in the whole spectrum and not at specific wavelengths, it is possible to take into account accurately the existing interactions in solution. For instance, the occurrence of complexation in solution can induce shifts in the spectra or potential changes in the molar absorptivity coefficient, that can be integrated in the multivariate calibration model. The UV-CD spectroscopy method could also be used for online monitoring of the solution composition during a crystallization process through in situ measurements, or solution sampling of the liquid phase concentration and enantiomeric excess. The advantages of the UV-CD method are the absorbance detection of both chiral and achiral molecules, unaffected by the sample temperature, facile method development and quick analysis. The sample preparation is minimal, requiring only sampling and dilution, and guarantees no possible physical/chemical degradation as it can be the case for other methods like chiral HPLC that introduces new solvents in contact with the sampled analytes. The same multivariate calibration models are needed for quantification of several components, and we prove the high consistency of data obtained through the present study. The limitations of the UV-CD method are the need for the molecules to absorb in the UV region, preferably in a region different from the solvent used. However, these criteria are already a requirement for chiral HPLC methods that use UV spectroscopy in their detectors. UV-CD cannot be applied to UV-sensitive molecules that become modified or degrade under UV light.<sup>79-81</sup> Other chiroptical techniques like Vibrational Circular Dichroism (VCD) or Raman

optical activity can be a good alternative to UV-CD,<sup>62</sup> as they present more pronounced spectra that arise from the vibration modes of the bonds, and thus are not limited by chemical degradation and absorption requirements. Both techniques also produce spectra, and therefore offer big possibilities in terms of data analysis with multivariate analysis to build quantification methods for chiral molecules.

## 5. Conclusions

---

A new multicomponent chiral quantification method using UV-Circular dichroism spectroscopy and PLS calibration models was created to measure unknown compositions in up to three different chiral components in solution, with two being enantiomers. This method was used to design calibration models covering the R/S/S-MA/MeCN quaternary system. Three accurate ternary phase diagrams were measured, revising previous literature data. Moreover, with the newly possible quaternary compositions quantification, the full quaternary phase diagram tetrahedron at 9°C was proposed for the first time. It shows the equilibria of the two enantiomers forming a racemic compound RS, and the enantiomer S forming an enantiospecific cocrystal S:S-MA with the chiral coformer S-MA. The calibration results show very high accuracy for models in predicting known compositions. They can predict total mass fraction in enantiomers  $x_{S+R}$  with a root mean square error of prediction (RMSEP) of  $16.3 \times 10^{-6}$  g/g, the differential mass fraction between enantiomers  $x_{S-R}$  with RMSEP of  $12.0 \times 10^{-6}$  g/g, and the mass fraction in S-MA  $x_{S-MA}$  with RMSEP of  $15.4 \times 10^{-6}$  g/g. The obtained phase diagram experimental results prove to be in good agreement with those obtained with other analytical methods such as HPLC and gravimetric analysis. The circular dichroism spectroscopy method is promising as it can be extended to wavelengths different from UV to build similar quantification models. Moreover, a higher number of different chiral molecules could be quantified in solution, with the appropriate multivariate calibration models on spectral data. Most chiral pharmaceutical compounds absorb in UV without degrading and their concentration tends to have an influence on the spectrum which is detectable by the PLS method in sufficient accuracy. Therefore, the method is potentially applicable to a large range of organic molecules. The accurate description of the quaternary phase diagram underlines a large asymmetry along the racemic composition, that shows the feasibility of a chiral separation process with enantioselective cocrystallization of levetiracetam under stable conditions. This highlights the necessity of complex multicomponent chiral phase diagram determination with precise methods, such as UV-CD spectroscopy and multivariate analysis.

## Associated content

---

### Supporting Information

The Supporting Information is available free of charge at ...

Materials, models development data, phase diagrams data.

### Data availability statement

All data underpinning this publication are openly available from the University of Strathclyde KnowledgeBase at: <https://doi.org/10.15129/414d46ee-fe46-4ec0-9cbb-67f29c5efdf6>



## Acknowledgements

---

This research received funding as part of the CORE ITN Project by the European Union's Horizon 2020 Research and Innovation Program under the Marie Skłodowska-Curie Grant Agreement No. 722456 CORE ITN. The authors thank the EPSRC Centre for Innovative Manufacturing in Continuous Manufacturing and Crystallization (<http://www.cmac.ac.uk>) for support (EPSRC funding under grant reference: EP/I033459/1). We thank UCB Pharma (Braine-l'Alleud, Belgium) for providing pure Levetiracetam, its counter-enantiomer, and racemic compound Etiracetam.

## References

---

- (1) Jacques, J.; Collet, A.; Wilen, S. H. *Enantiomers, racemates, and resolutions*; Wiley, 1981.
- (2) Nguyen, L. A.; He, H.; Pham-Huy, C. Chiral drugs: an overview. *Int J Biomed Sci* **2006**, 2 (2), 85-100.
- (3) Reddy, I. K.; Mehvar, R. *Chirality in drug design and development*; CRC Press, 2004.
- (4) Saigo, K.; Sakai, K. Resolution of chiral drugs and drug intermediates by crystallisation. *Chirality in drug research* **2006**, 127-154.
- (5) Li, Z. J.; Grant, D. J. Relationship between physical properties and crystal structures of chiral drugs. *J Pharm Sci* **1997**, 86 (10), 1073-1078.
- (6) Ariens, E. J. Stereochemistry, a basis for sophisticated nonsense in pharmacokinetics and clinical pharmacology. *Eur J Clin Pharmacol* **1984**, 26 (6), 663-668.
- (7) Kenda, B. M.; Matagne, A. C.; Talaga, P. E.; Pasau, P. M.; Differding, E.; Lallemand, B. I.; Frycia, A. M.; Moureau, F. G.; Klitgaard, H. V.; Gillard, M. R.; et al. Discovery of 4-Substituted Pyrrolidone Butanamides as New Agents with Significant Antiepileptic Activity. *Journal of Medicinal Chemistry* **2004**, 47 (3), 530-549.
- (8) van der Meijden, M. W.; Leeman, M.; Gelens, E.; Noorduyn, W. L.; Meekes, H.; van Enkevort, W. J. P.; Kaptein, B.; Vlieg, E.; Kellogg, R. M. Attrition-Enhanced Deracemization in the Synthesis of Clopidogrel - A Practical Application of a New Discovery. *Organic Process Research & Development* **2009**, 13 (6), 1195-1198.
- (9) Suwannasang, K.; Flood, A. E.; Coquerel, G. A Novel Design Approach To Scale Up the Temperature Cycle Enhanced Deracemization Process: Coupled Mixed-Suspension Vessels. *Crystal Growth & Design* **2016**, 16 (11), 6461-6467.
- (10) Sheldon, R. A. *Chirotechnology: industrial synthesis of optically active compounds*; CRC press, 1993.
- (11) Belletti, G.; Tortora, C.; Mellema, I. D.; Tinnemans, P.; Meekes, H.; Rutjes, F.; Tsogoeva, S. B.; Vlieg, E. Photoracemization-Based Viedma Ripening of a BINOL Derivative. *Chemistry* **2020**, 26 (4), 839-844.
- (12) Sakai, K.; Hirayama, N.; Tamura, R. *Novel optical resolution technologies*; Springer, 2007.
- (13) Suwannasang, K.; Flood, A. E.; Rougeot, C.; Coquerel, G. Using Programmed Heating-Cooling Cycles with Racemization in Solution for Complete Symmetry Breaking of a Conglomerate Forming System. *Crystal Growth & Design* **2013**, 13 (8), 3498-3504.
- (14) Li, W. W.; Spix, L.; de Reus, S. C. A.; Meekes, H.; Kramer, H. J. M.; Vlieg, E.; ter Horst, J. H. Deracemization of a Racemic Compound via Its Conglomerate-Forming Salt Using Temperature Cycling. *Crystal Growth & Design* **2016**, 16 (9), 5563-5570.
- (15) Sogutoglu, L. C.; Steendam, R. R.; Meekes, H.; Vlieg, E.; Rutjes, F. P. Viedma ripening: a reliable crystallisation method to reach single chirality. *Chem Soc Rev* **2015**, 44 (19), 6723-6732.
- (16) Buol, X.; Caro Garrido, C.; Robeyns, K.; Tumanov, N.; Collard, L.; Wouters, J.; Leyssens, T. Chiral Resolution of Mandelic Acid through Preferential Cocrystallization with Nefiracetam. *Crystal Growth & Design* **2020**, 20 (12), 7979-7988.
- (17) Lorenz, H.; Seidel-Morgenstern, A. Processes to separate enantiomers. *Angew Chem Int Ed Engl* **2014**, 53 (5), 1218-1250.

- (18) Kellogg, R. M. Practical Stereochemistry. *Acc Chem Res* **2017**, 50 (4), 905-914.
- (19) Maggioni, G. M.; Fernández-Ronco, M. P.; van der Meijden, M. W.; Kellogg, R. M.; Mazzotti, M. Solid state deracemisation of two imine-derivatives of phenylglycine derivatives via high-pressure homogenisation and temperature cycles. *CrystEngComm* **2018**, 20 (27), 3828-3838.
- (20) Breveglieri, F.; Maggioni, G. M.; Mazzotti, M. Deracemization of NMPA via Temperature Cycles. *Crystal Growth & Design* **2018**, 18 (3), 1873-1881.
- (21) Belletti, G.; Meekes, H.; Rutjes, F.; Vlieg, E. Role of Additives during Deracemization Using Temperature Cycling. *Cryst Growth Des* **2018**, 18 (11), 6617-6620.
- (22) Levilain, G.; Coquerel, G. Pitfalls and rewards of preferential crystallization. *CrystEngComm* **2010**, 12 (7), 1983-1992.
- (23) Harfouche, L. C.; Brandel, C.; Cartigny, Y.; Ter Horst, J. H.; Coquerel, G.; Petit, S. Enabling Direct Preferential Crystallization in a Stable Racemic Compound System. *Mol Pharm* **2019**, 16 (11), 4670-4676.
- (24) Kozma, D. *CRC handbook of optical resolutions via diastereomeric salt formation*; Crc Press, 2001.
- (25) Marchand, P.; Lefebvre, L.; Querniard, F.; Cardinael, P.; Perez, G.; Counieux, J. J.; Coquerel, G. Diastereomeric resolution rationalized by phase diagrams under the actual conditions of the experimental process. *Tetrahedron-Asymmetry* **2004**, 15 (16), 2455-2465.
- (26) Lam, W. H.; Ng, K. M. Diastereomeric salt crystallization synthesis for chiral resolution of ibuprofen. *Aiche Journal* **2007**, 53 (2), 429-437.
- (27) Harfouche, L. C.; Couvrat, N.; Sanselme, M.; Brandel, C.; Cartigny, Y.; Petit, S.; Coquerel, G. Discovery of New Proxyphylline-Based Chiral Cocrystals: Solid State Landscape and Dehydration Mechanism. *Crystal Growth & Design* **2020**, 20 (6), 3842-3850.
- (28) Neurohr, C.; Marchivie, M.; Lecomte, S.; Cartigny, Y.; Couvrat, N.; Sanselme, M.; Subra-Paternault, P. Naproxen-Nicotinamide Cocrystals: Racemic and Conglomerate Structures Generated by CO<sub>2</sub> Antisolvent Crystallization. *Crystal Growth & Design* **2015**, 15 (9), 4616-4626.
- (29) Wacharine-Antar, S.; Levilain, G.; Dupray, V.; Coquerel, G. Resolution of (+/-)-Imeglimin-2,4-dichlorophenylacetate Methanol Solvate by Preferential Crystallization. *Organic Process Research & Development* **2010**, 14 (6), 1358-1363.
- (30) Guillot, M.; de Meester, J.; Huynen, S.; Collard, L.; Robeyns, K.; Riant, O.; Leyssens, T. Cocrystallization-Induced Spontaneous Deracemization: A General Thermodynamic Approach to Deracemization. *Angew Chem Int Ed Engl* **2020**, 59 (28), 11303-11306.
- (31) Springuel, G.; Leyssens, T. Innovative Chiral Resolution Using Enantiospecific Co-Crystallization in Solution. *Crystal Growth & Design* **2012**, 12 (7), 3374-3378.
- (32) Harmsen, B.; Leyssens, T. Dual-Drug Chiral Resolution: Enantiospecific Cocrystallization of (S)-Ibuprofen Using Levetiracetam. *Crystal Growth & Design* **2017**, 18 (1), 441-448.
- (33) Harmsen, B.; Leyssens, T. Enabling Enantiopurity: Combining Racemization and Dual-Drug Co-crystal Resolution. *Crystal Growth & Design* **2018**, 18 (6), 3654-3660.
- (34) Springuel, G.; Robeyns, K.; Norberg, B.; Wouters, J.; Leyssens, T. Cocrystal Formation between Chiral Compounds: How Cocrystals Differ from Salts. *Crystal Growth & Design* **2014**, 14 (8), 3996-4004.
- (35) Harmsen, B.; Leyssens, T. Dual-Drug Chiral Resolution: Enantiospecific Cocrystallization of (S)-Ibuprofen Using Levetiracetam. *Crystal Growth & Design* **2018**, 18 (1), 441-448.
- (36) Springuel, G.; Collard, L.; Leyssens, T. Ternary and quaternary phase diagrams: key tools for chiral resolution through solution cocrystallization. *Crystengcomm* **2013**, 15 (39), 7951-7958.
- (37) Mullin, J. W. *Crystallization*; Elsevier, 2001.
- (38) Coquerel, G. Crystallization of molecular systems from solution: phase diagrams, supersaturation and other basic concepts. *Chem Soc Rev* **2014**, 43 (7), 2286-2300.
- (39) Cascella, F.; Seidel-Morgenstern, A.; Lorenz, H. Exploiting Ternary Solubility Phase Diagrams for Resolution of Enantiomers: An Instructive Example. *Chemical Engineering & Technology* **2020**, 43 (2), 329-336.

- (40) Brandel, C.; Amharar, Y.; Rollinger, J. M.; Griesser, U. J.; Cartigny, Y.; Petit, S.; Coquerel, G. Impact of molecular flexibility on double polymorphism, solid solutions and chiral discrimination during crystallization of diprophylline enantiomers. *Mol Pharm* **2013**, *10* (10), 3850-3861.
- (41) Lorenz, H.; Seidel-Morgenstern, A. Binary and ternary phase diagrams of two enantiomers in solvent systems. *Thermochimica Acta* **2002**, *382* (1-2), 129-142.
- (42) Polenske, D.; Lorenz, H. Solubility and Metastable Zone Width of the Methionine Enantiomers and Their Mixtures in Water. *Journal of Chemical and Engineering Data* **2009**, *54* (8), 2277-2280.
- (43) Leyssens, T.; ter Horst, J. H. 9. Solution co-crystallisation and its applications. In *Multi-Component Crystals*, De Gruyter, 2017; pp 205-236.
- (44) Song, L.; Leng, F.; Robeyns, K.; Leyssens, T. Quaternary phase diagrams as a tool for ionic cocrystallization: the case of a solid solution between a racemic and enantiopure ionic cocrystal. *CrystEngComm* **2020**, *22* (14), 2537-2542.
- (45) Zhou, F.; Shemchuk, O.; Charpentier, M. D.; Matheys, C.; Collard, L.; Ter Horst, J. H.; Leyssens, T. Simultaneous Chiral Resolution of Two Racemic Compounds by Preferential Cocrystallization\*. *Angew Chem Int Ed Engl* **2021**, *60* (37), 20264-20268.
- (46) Buol, X.; Robeyns, K.; Caro Garrido, C.; Tumanov, N.; Collard, L.; Wouters, J.; Leyssens, T. Improving Nefiracetam Dissolution and Solubility Behavior Using a Cocrystallization Approach. *Pharmaceutics* **2020**, *12* (7),
- (47) Alvarez Rodrigo, A.; Lorenz, H.; Seidel-Morgenstern, A. Online monitoring of preferential crystallization of enantiomers. *Chirality* **2004**, *16* (8), 499-508.
- (48) Hughes, D.; Carreira, E.; Yamamoto, H. Comprehensive Chirality. *Carreira, EM* **2012**,
- (49) Gawley, R. E.; Aubé, J. *Principles of asymmetric synthesis*; Elsevier, 2012.
- (50) Hanna, G. M. Determination of enantiomeric composition of ibuprofen in bulk drug by proton nuclear magnetic resonance spectroscopy with a chiral lanthanide chelate. *J Pharm Biomed Anal* **1997**, *15* (12), 1805-1811.
- (51) Oketani, R.; Marin, F.; Tinnemans, P.; Hoquante, M.; Laurent, A.; Brandel, C.; Cardinael, P.; Meekes, H.; Vlieg, E.; Geerts, Y.; et al. Deracemization in a Complex Quaternary System with a Second-Order Asymmetric Transformation by Using Phase Diagram Studies. *Chemistry* **2019**, *25* (61), 13890-13898.
- (52) Buol, X.; Robeyns, K.; Caro Garrido, C.; Tumanov, N.; Collard, L.; Wouters, J.; Leyssens, T. Improving Nefiracetam Dissolution and Solubility Behavior Using a Cocrystallization Approach. *Pharmaceutics* **2020**, *12* (7), 653.
- (53) Buol, X.; Garrido, C. C.; Robeyns, K.; Tumanov, N.; Collard, L.; Wouters, J.; Leyssens, T. Chiral Resolution of Mandelic Acid through Preferential Cocrystallization with Nefiracetam. *Crystal Growth & Design* **2020**, *20* (12), 7979-7988.
- (54) Hegade, R. S.; De Beer, M.; Lynen, F. Chiral stationary phase optimized selectivity liquid chromatography: A strategy for the separation of chiral isomers. *J Chromatogr A* **2017**, *1515*, 109-117.
- (55) Berova, N.; Polavarapu, P. L.; Nakanishi, K.; Woody, R. W. *Comprehensive chiroptical spectroscopy: applications in stereochemical analysis of synthetic compounds, natural products, and biomolecules*; John Wiley & Sons, 2012.
- (56) Berova, N.; Nakanishi, K.; Woody, R. W. *Circular dichroism: principles and applications*; John Wiley & Sons, 2000.
- (57) Polavarapu, P. L. *Chiroptical spectroscopy: fundamentals and applications*; Crc Press, 2016.
- (58) Liu, M.; Chen, L.; Tian, T.; Zhang, Z.; Li, X. Identification and Quantitation of Enantiomers by Capillary Electrophoresis and Circular Dichroism Independent of Single Enantiomer Standard. *Anal Chem* **2019**, *91* (21), 13803-13809.
- (59) Luo, Y.; Wu, L.; Yang, B.; Jin, Y.; Zheng, K.; He, Z. A novel potential primary method for quantification of enantiomers by high performance liquid chromatography-circular dichroism. *Sci Rep* **2018**, *8* (1), 7390.

- (60) Nieto, S.; Dragna, J. M.; Anslyn, E. V. A facile CD protocol for rapid determination of enantiomeric excess and concentration of chiral primary amines. *Chemistry* **2010**, *16* (1), 227.
- (61) Jo, H. H.; Lin, C. Y.; Anslyn, E. V. Rapid optical methods for enantiomeric excess analysis: from enantioselective indicator displacement assays to exciton-coupled circular dichroism. *Acc Chem Res* **2014**, *47* (7), 2212-2221.
- (62) Berova, N.; Polavarapu, P. L.; Nakanishi, K.; Woody, R. W. *Comprehensive Chiroptical Spectroscopy: Instrumentation, Methodologies, and Theoretical Simulations*; John Wiley & Sons, 2011.
- (63) Bakeev, K. A. *Process analytical technology: spectroscopic tools and implementation strategies for the chemical and pharmaceutical industries*; John Wiley & Sons, 2010.
- (64) Simone, E.; Saleemi, A. N.; Nagy, Z. K. Application of quantitative Raman spectroscopy for the monitoring of polymorphic transformation in crystallization processes using a good calibration practice procedure. *Chemical Engineering Research & Design* **2014**, *92* (4), 594-611.
- (65) Morais, C. L. M.; Santos, M. C. D.; Lima, K. M. G.; Martin, F. L. Improving data splitting for classification applications in spectrochemical analyses employing a random-mutation Kennard-Stone algorithm approach. *Bioinformatics* **2019**, *35* (24), 5257-5263.
- (66) Winning, H.; Larsen, F. H.; Bro, R.; Engelsen, S. B. Quantitative analysis of NMR spectra with chemometrics. *J Magn Reson* **2008**, *190* (1), 26-32.
- (67) Brereton, R. G. *Chemometrics: data driven extraction for science*; John Wiley & Sons, 2018.
- (68) Swinehart, D. F. The beer-lambert law. *Journal of chemical education* **1962**, *39* (7), 333.
- (69) Adams, M. J. *Chemometrics in analytical spectroscopy*; Royal Society of Chemistry, 2004.
- (70) Mower, M. P.; Blackmond, D. G. In-Situ Monitoring of Enantiomeric Excess During a Catalytic Kinetic Resolution. *Acs Catalysis* **2018**, *8* (7), 5977-5982.
- (71) Bro, R. Multivariate calibration: what is in chemometrics for the analytical chemist? *Analytica Chimica Acta* **2003**, *500* (1-2), 185-194.
- (72) Haenlein, M.; Kaplan, A. M. A beginner's guide to partial least squares analysis. *Understanding statistics* **2004**, *3* (4), 283-297.
- (73) Savitzky, A.; Golay, M. J. E. Smoothing + Differentiation of Data by Simplified Least Squares Procedures. *Analytical Chemistry* **1964**, *36* (8), 1627-&.
- (74) Alexandris, N.; Gupta, S.; Koutsias, N. Remote sensing of burned areas via PCA, Part 1; centering, scaling and EVD vs SVD. *Open geospatial data, software and standards* **2017**, *2* (1), 1-11.
- (75) Galvao, R. K.; Araujo, M. C.; Jose, G. E.; Pontes, M. J.; Silva, E. C.; Saldanha, T. C. A method for calibration and validation subset partitioning. *Talanta* **2005**, *67* (4), 736-740.
- (76) Frank, L. E.; Friedman, J. H. A statistical view of some chemometrics regression tools. *Technometrics* **1993**, *35* (2), 109-135.
- (77) Nehm, S. J.; Rodríguez-Spong, B.; Rodríguez-Hornedo, N. Phase Solubility Diagrams of Cocrystals Are Explained by Solubility Product and Solution Complexation. *Crystal Growth & Design* **2006**, *6* (2), 592-600.
- (78) Ricci, J. E. *phase rule and heterogeneous equilibrium*; 1951.
- (79) Wypych, G. *Handbook of UV degradation and stabilization*; Elsevier, 2020.
- (80) Wang, W. L.; Zhang, X.; Wu, Q. Y.; Du, Y.; Hu, H. Y. Degradation of natural organic matter by UV/chlorine oxidation: Molecular decomposition, formation of oxidation byproducts and cytotoxicity. *Water Res* **2017**, *124*, 251-258.
- (81) Zayat, M.; Garcia-Parejo, P.; Levy, D. Preventing UV-light damage of light sensitive materials using a highly protective UV-absorbing coating. *Chem Soc Rev* **2007**, *36* (8), 1270-1281.

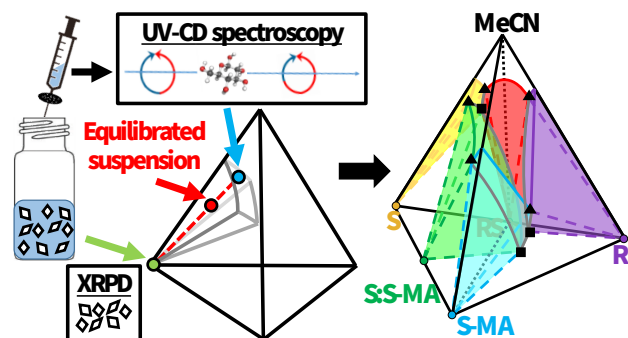
## For Table of Contents Use Only

---

Manuscript title: Multicomponent chiral quantification with UV circular dichroism spectroscopy: ternary and quaternary phase diagrams of Levetiracetam

Author list: Maxime D. Charpentier, Raghunath Venkatramanan, Céline Rougeot, Tom Leysens, Karen Johnston, Joop H. ter Horst

TOC graphic:



Synopsis for TOC: use "Abstract" section

Keywords: Cocrystals ; Phase diagrams ; Crystallization ; Chirality ; Pharmaceuticals ; Solubility

# Supporting Information:

## “Multicomponent chiral quantification with UV circular dichroism spectroscopy: ternary and quaternary phase diagrams of Levetiracetam”

**Maxime D. Charpentier**<sup>1</sup>, Raghunath Venkatramanan<sup>1</sup>, Céline Rougeot<sup>2</sup>, Tom Leyssens<sup>3</sup>, Karen Johnston<sup>4</sup>, Joop H. ter Horst<sup>1,5</sup>

1. EPSRC Centre for Innovative Manufacturing in Continuous Manufacturing and Crystallization (CMAC), University of Strathclyde, Technology and Innovation Centre, 99 George Street, Glasgow G1 1RD, U.K.

2. UCB Pharma SA, chemin du Foriest, 1420 Braine-L'Alleud, Belgium

3. Institute of Condensed Matter and Nanosciences, UCLouvain, Place L. Pasteur 1, Belgium.

4. Department of Chemical and Process Engineering, University of Strathclyde, James Weir Building, 75 Montrose Street, Glasgow G1 1XJ, U.K.

5. Univ Rouen Normandie, Laboratoire Sciences et Méthodes Séparatives (SMS), UR 3233, F-76000 Rouen, France

### Table of contents

S1 – Materials	2
S2 – Model development data	3
S3 – Phase diagrams data	11

## S1 - Materials

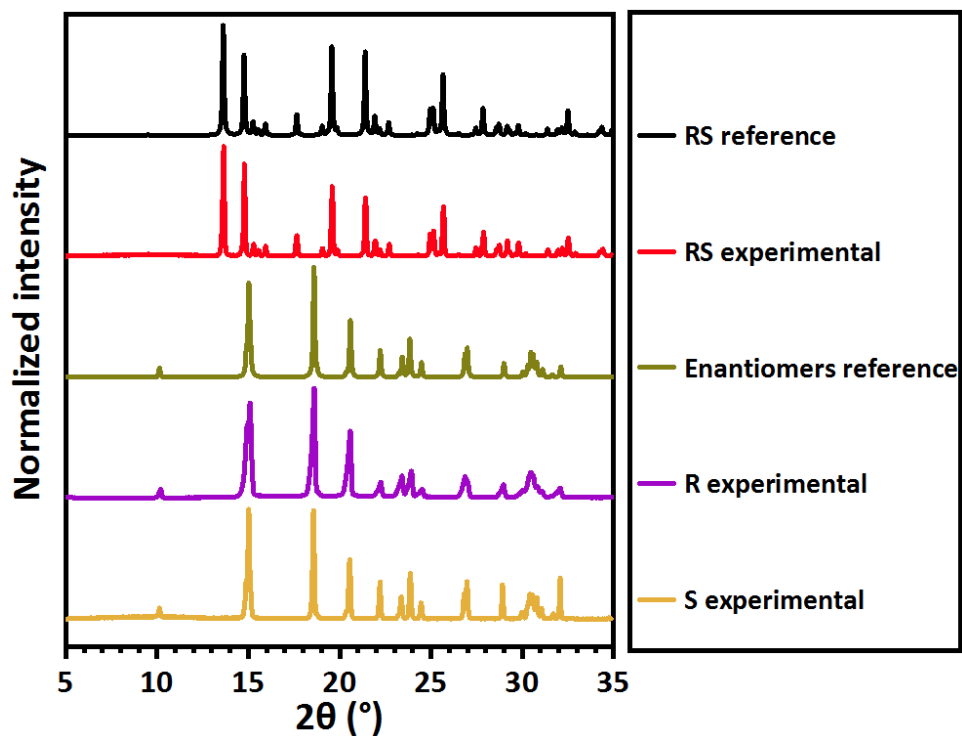


Figure S13: Experimental and reference XRPD patterns for solids of both enantiomers, and racemic compound RS.

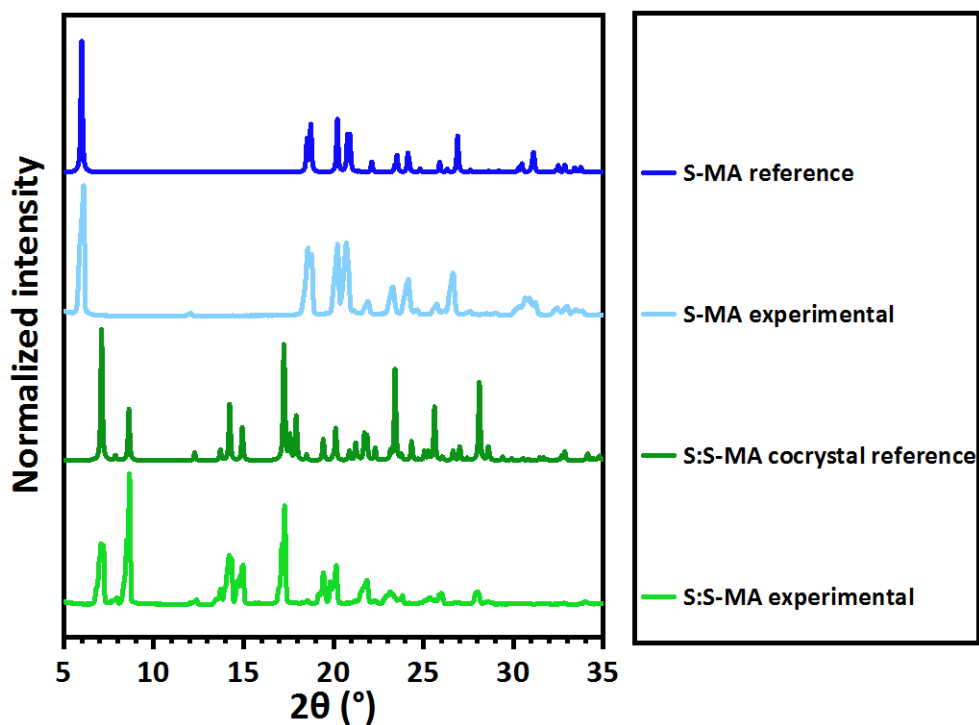


Figure S14: Experimental and reference XRPD patterns for solids of S:S-MA cocrystal and S-MA.

## S2 – Multivariate calibration model development data

### S2.1 – Mass fractions of calibration samples used

**Table S2:** Components mass fractions of calibration samples prepared in MeCN used for the calibration model.

Section	$x_R$	$x_S$	$x_{S-MA}$
Ternary R/S/MeCN	0	0.001266	0
	0	0.002657	0
	0	0.003947	0
	0	0.005210	0
	0	0.006307	0
	0.000115	0.001126	0
	0.000226	0.002213	0
	0.000348	0.003403	0
	0.000464	0.004538	0
	0.000580	0.005668	0
	0.000243	0.000990	0
	0.000492	0.001999	0
	0.000740	0.003008	0
	0.000985	0.004007	0
	0.001230	0.005004	0
	0.000381	0.000897	0
	0.000764	0.001801	0
	0.001150	0.002710	0
	0.001533	0.003612	0
	0.001915	0.004513	0
	0.000518	0.000813	0
	0.001038	0.001629	0
	0.001557	0.002444	0
	0.002080	0.003265	0
	0.002598	0.004078	0
	0.000636	0.000636	0
	0.001286	0.001286	0
	0.001931	0.001931	0
	0.002578	0.002578	0
	0.003219	0.003219	0
	0.001266	0	0
	0.002657	0	0
	0.003947	0	0
	0.005210	0	0
	0.006307	0	0
	0.001126	0.000115	0
	0.002213	0.000226	0



	0.003403	0.000348	0
	0.004538	0.000464	0
	0.005668	0.000580	0
	0.000990	0.000243	0
	0.001999	0.000492	0
	0.003008	0.000740	0
	0.004007	0.000985	0
	0.005004	0.001230	0
	0.000897	0.000381	0
	0.001801	0.000764	0
	0.002710	0.001150	0
	0.003612	0.001533	0
	0.004513	0.001915	0
	0.000813	0.000518	0
	0.001629	0.001038	0
	0.002444	0.001557	0
	0.003265	0.002080	0
	0.004078	0.002598	0
Ternary S/SMA/MeCN	0	0	0.001197
	0	0	0.002379
	0	0	0.003604
	0	0	0.004751
	0	0	0.005964
	0	0.000296	0.000936
	0	0.000608	0.001922
	0	0.000917	0.002900
	0	0.001238	0.003916
	0	0.001555	0.004918
	0	0.000460	0.000808
	0	0.000924	0.001625
	0	0.001395	0.002452
	0	0.001859	0.003268
	0	0.002334	0.004103
	0	0.000743	0.000527
	0	0.001490	0.001057
	0	0.002220	0.001575
	0	0.002982	0.002115
	0	0.003721	0.002640
	0	0.000942	0.000261
	0	0.001941	0.000537
	0	0.002900	0.000802
	0	0.003832	0.001060
	0	0.004807	0.001329

	0	0.001248	0
	0	0.002465	0
	0	0.003723	0
	0	0.004978	0
	0	0.006244	0
	0	0.000180	0.001131
	0	0.000352	0.002214
	0	0.000527	0.003310
	0	0.000704	0.004427
	0	0.000889	0.005590
	0	0.000355	0.000903
	0	0.000713	0.001817
	0	0.001041	0.002652
	0	0.001405	0.003579
	0	0.001763	0.004490
	0	0.000684	0.000616
	0	0.001371	0.001235
	0	0.002046	0.001842
	0	0.002734	0.002461
	0	0.003426	0.003084
	0	0.000893	0.000465
	0	0.001759	0.000916
	0	0.002650	0.001381
	0	0.003553	0.001852
	0	0.004457	0.002323
	0	0.001100	0.000126
	0	0.002206	0.000252
	0	0.003314	0.000379
	0	0.004422	0.000506
	0	0.005550	0.000635
Ternary R/SMA/MeCN	0.000136	0	0.001150
	0.000276	0	0.002330
	0.000416	0	0.003507
	0.000554	0	0.004668
	0.000242	0	0.001049
	0.000490	0	0.002124
	0.000737	0	0.003193
	0.000982	0	0.004254
	0.000354	0	0.000844
	0.000716	0	0.001710
	0.001080	0	0.002579
	0.001440	0	0.003436
	0.000522	0	0.000742

	0.001054	0	0.001499
	0.001587	0	0.002256
	0.002113	0	0.003005
	0.000655	0	0.000649
	0.001316	0	0.001303
	0.001960	0	0.001942
	0.002645	0	0.002620
	0.000663	0	0.000429
	0.001335	0	0.000864
	0.002004	0	0.001296
	0.002676	0	0.001731
	0.003344	0	0.002163
	0.000755	0	0.000319
	0.001523	0	0.000643
	0.002285	0	0.000965
	0.003055	0	0.001290
	0.003813	0	0.001610
	0.000831	0	0.000200
	0.001673	0	0.000403
	0.002518	0	0.000607
	0.003356	0	0.000808
	0.004191	0	0.001010
	0.000942	0	0.000115
	0.001884	0	0.000229
	0.002822	0	0.000344
	0.003764	0	0.000458
	0.004703	0	0.000573
Quaternary	0.000492	0.000492	0.000495
	0.000978	0.000978	0.000984
	0.001467	0.001467	0.001476
	0.001950	0.001950	0.001962
	0.000330	0.000330	0.000944
	0.000656	0.000656	0.001874
	0.000981	0.000981	0.002803
	0.001309	0.001309	0.003739
	0.000149	0.000149	0.001218
	0.000297	0.000297	0.002422
	0.000448	0.000448	0.003646
	0.000597	0.000597	0.004859
	0.000678	0.000678	0.000296
	0.001340	0.001340	0.000585
	0.002019	0.002019	0.000881
	0.002682	0.002682	0.001171

	0.000322	0.000970	0.000327
	0.000646	0.001945	0.000656
	0.000985	0.002965	0.001000
	0.001290	0.003884	0.001310
	0.000128	0.000971	0.000154
	0.000257	0.001948	0.000308
	0.000384	0.002911	0.000460
	0.000515	0.003908	0.000618
	0.000642	0.004874	0.000771
	0.000165	0.000830	0.000321
	0.000329	0.001649	0.000639
	0.000491	0.002464	0.000954
	0.000656	0.003292	0.001275
	0.000820	0.004117	0.001595
	0.000123	0.000577	0.000521
	0.000244	0.001148	0.001037
	0.000369	0.001737	0.001569
	0.000495	0.002328	0.002102
	0.000621	0.002922	0.002638
	0.000116	0.000330	0.000794
	0.000234	0.000664	0.001599
	0.000352	0.001001	0.002411
	0.000474	0.001347	0.003242
	0.000595	0.001691	0.004072
	0.000258	0.000522	0.000519
	0.000506	0.001024	0.001018
	0.000760	0.001539	0.001530
	0.001020	0.002064	0.002052
	0.001284	0.002599	0.002584
	0.000442	0.000713	0.000195
	0.000868	0.001400	0.000383
	0.001312	0.002115	0.000579
	0.001746	0.002815	0.000771
	0.002168	0.003495	0.000957
	0.000657	0.000235	0.000218
	0.001320	0.000472	0.000439
	0.001989	0.000711	0.000662
	0.002651	0.000947	0.000882
	0.003310	0.001183	0.001101
	0.000860	0.000113	0.000103
	0.001723	0.000227	0.000206
	0.002594	0.000342	0.000310
	0.003467	0.000457	0.000414

	0.004321	0.000570	0.000516
	0.000680	0.000105	0.000298
	0.001373	0.000213	0.000601
	0.002060	0.000319	0.000902
	0.002750	0.000426	0.001205
	0.003433	0.000532	0.001504
	0.000490	0.000144	0.000475
	0.000989	0.000289	0.000959
	0.001488	0.000436	0.001443
	0.001981	0.000580	0.001921
	0.002474	0.000724	0.002399
	0.000362	0.000098	0.000672
	0.000725	0.000197	0.001347
	0.001092	0.000297	0.002029
	0.001455	0.000396	0.002703
	0.001817	0.000494	0.003375
	0.000448	0.000216	0.000424
	0.000901	0.000435	0.000852
	0.001350	0.000652	0.001276
	0.001803	0.000871	0.001705
	0.002250	0.001087	0.002128
	0.000663	0.000360	0.000110
	0.001338	0.000726	0.000223
	0.002007	0.001090	0.000334
	0.002677	0.001453	0.000445
	0.003343	0.001814	0.000556
	0.000621	0.000207	0.000269
	0.001260	0.000420	0.000546
	0.001891	0.000630	0.000820
	0.002525	0.000842	0.001095
	0.003151	0.001050	0.001366
	0.000825	0.000100	0.000100
	0.001657	0.000201	0.000201
	0.002487	0.000301	0.000301
	0.003320	0.000402	0.000402
	0.004137	0.000501	0.000501
	0.000638	0.000125	0.000314
	0.001279	0.000251	0.000630
	0.001922	0.000377	0.000946
	0.002569	0.000505	0.001264
	0.003207	0.000630	0.001578
	0.000484	0.000106	0.000457
	0.000975	0.000212	0.000920

	0.001463	0.000319	0.001380
	0.001955	0.000426	0.001845
	0.002437	0.000531	0.002298
	0.000308	0.000093	0.000611
	0.000618	0.000187	0.001224
	0.000930	0.000281	0.001842
	0.001240	0.000374	0.002456
	0.001547	0.000467	0.003065
	0.000389	0.000194	0.000405
	0.000787	0.000392	0.000818
	0.001189	0.000592	0.001236
	0.001586	0.000790	0.001650
	0.001980	0.000987	0.002059
	0.000640	0.000349	0.000094
	0.001269	0.000693	0.000187
	0.001922	0.001049	0.000282
	0.002560	0.001397	0.000376
	0.003197	0.001744	0.000470

## S2.2 – Models validation by comparing results with gravimetric method

**Table S2:** Comparison of results obtained from UV-CD calibration method and gravimetry on the same 28 solutions of varying compositions in S and S-MA. The percentage error  $\delta$  (%) =  $\frac{|X - Y|}{Y}$  is used, with X being the total solubility obtained with UV-CD models result, and Y the total solubility from gravimetric method, on the same saturated solution.

Mass fraction total solid X (UV-CD)	Mass fraction total solid Y (Gravimetry)	Percentage Error $\delta$ (%)
0.037	0.037	0.294
0.038	0.038	0.198
0.040	0.039	0.361
0.138	0.133	3.528
0.139	0.137	1.912
0.135	0.132	2.168
0.213	0.214	0.459
0.224	0.227	1.261
0.216	0.214	0.567
0.236	0.234	0.725
0.245	0.241	1.583
0.240	0.236	1.982
0.258	0.254	1.444
0.270	0.288	6.368
0.099	0.095	4.283
0.105	0.101	3.634
0.117	0.114	2.463
0.110	0.107	2.341
0.125	0.123	2.206
0.118	0.116	1.599
0.114	0.113	0.861
0.114	0.111	2.636
0.114	0.112	2.136
0.128	0.122	4.468
0.118	0.121	2.507
0.135	0.13	3.881
0.140	0.136	2.507
0.152	0.152	0.192
<b>Average percentage error <math>\delta</math></b>		<b>2.091</b>
<b>Standard deviation</b>		<b>1.472</b>

### S3 – Phase diagrams data

**Table S3:** Solubilities of pure solid phases, eutectic points in ternary sections and quaternary points from the quaternary system R/S/S-MA/MeCN results at 9°C. Pure R, S and S-MA solubilities are the average of four compositions points. Pure RS and pure S:S-MA solubilities are computed from extrapolation of solubility curves. Points a, b and c were found experimentally. Points d, e and f were estimated from intersection of neighbouring solubility curves or surfaces. Points g and h could not be determined because of very high viscosity of saturated solutions in the region they belong, therefore only a roughly estimated compositional region is proposed.

Solubility at 9°C	Molar fraction X in dissolved components (%mol)	Mass concentration (mg/mL MeCN)
Pure R and S	R/S: 0.933	R/S: 30.7
Pure RS	R: 0.302 S: 0.302 Total: 0.604	R: 9.9 S: 9.9 Total: 19.8
Pure S-MA (average)	S-MA: 4.054	S-MA: 123.2
Pure S:S-MA	S: 1.591 S-MA: 1.591 Total: 3.182	S: 53.6 S-MA: 47.9 Total: 101.5
Eutectic point <b>a</b> (equilibrium with R and RS)	R: 0.954 S: 0.134 Total: 1.088	R: 31.4 S: 4.4 Total: 35.8
Eutectic point <b>b</b> (equilibrium with RS and S)	R: 0.134 S: 0.954 Total: 1.088	R: 4.4 S: 31.4 Total: 35.8
Eutectic point <b>c</b> (equilibrium with S and S:S-MA)	S: 1.974 S-MA: 1.253 Total: 3.227	S: 66.5 S-MA: 37.7 Total: 102.2
Eutectic point <b>d</b> (equilibrium with S:S-MA and S-MA)	S: 1.799 S-MA: 7.132 Total: 8.931	S: 64.4 S-MA: 228.2 Total: 292.6
Eutectic point <b>e</b> (equilibrium with R and S-MA)	R: 29.5 S-MA: 36.5 Total: 66.0	R: 2827.7 S-MA: 3127.4 Total: 5955.1
Quaternary point <b>f</b> (equilibrium with S, RS and S:S-MA)	R: 0.356 S: 2.176 S-MA: 1.513 Total: 4.045	R: 12.1 S: 73.9 S-MA: 45.9 Total: 131.9



Quaternary point <b>g</b> (equilibrium with R, RS and S-MA)	<b>Solvent-free ratio</b> R: 38.1% S: 8.1% S-MA: 53.8%	Total solubility > 6000 mg/mL MeCN
Quaternary point <b>h</b> (equilibrium with RS, S-MA and S:S-MA)	<b>Solvent-free ratio</b> R: 43.0% S: 6.0% S-MA: 51.0%	Total solubility > 6000 mg/mL MeCN

### S3.1 – Isothermal ternary system between enantiomers R and S

**Table S4:** Data used for the ternary phase diagram R/S/MeCN at 9°C.

Model prediction from UV-CD			Dilution	Final liquid composition (molar fraction)			Solid
$X_{S+R}$ of diluted solution	$X_{S-R}$ of diluted solution	Enantiomeric excess $E$ of diluted solution (%)	Dilution ratio	$X_R$ (%)	$X_S$ (%)	$X_{MeCN}$ (%)	Solid phase(s) in suspension (XRPD)
0.00336	0.00336	100.00	10.667	0.000	0.889	99.111	S
0.00333	0.00310	93.07	12.045	0.035	0.964	99.002	S
0.00369	0.00328	88.78	10.573	0.054	0.916	99.029	S
0.00375	0.00320	85.41	10.643	0.072	0.920	99.008	S
0.00380	0.00300	78.94	11.104	0.111	0.942	98.947	S
0.00396	0.00302	76.16	10.915	0.129	0.950	98.922	S
0.00385	0.00290	75.33	11.335	0.134	0.954	98.911	S + RS
0.00396	0.00289	73.08	10.913	0.145	0.933	98.922	RS
0.00372	0.00265	71.14	10.813	0.144	0.857	98.999	RS
0.00351	0.00240	68.49	11.213	0.154	0.825	99.021	RS
0.00360	0.00248	68.98	11.040	0.153	0.835	99.012	RS
0.00287	0.00187	65.08	12.698	0.158	0.745	99.097	RS
0.00261	0.00170	65.09	12.930	0.146	0.689	99.165	RS
0.00331	0.00209	63.05	10.922	0.166	0.731	99.103	RS
0.00281	0.00163	57.92	12.332	0.180	0.677	99.143	RS
0.00287	0.00155	54.11	11.431	0.186	0.625	99.189	RS
0.00234	0.00129	55.02	11.603	0.150	0.518	99.332	RS
0.00255	0.00123	48.17	12.401	0.202	0.578	99.220	RS
0.00257	0.00109	42.52	11.329	0.207	0.512	99.281	RS
0.00240	0.00096	40.10	11.116	0.197	0.460	99.343	RS
0.00230	0.00075	32.68	11.276	0.214	0.422	99.363	RS
0.00232	0.00063	27.11	10.926	0.227	0.395	99.378	RS
0.00218	0.00040	18.42	11.430	0.250	0.363	99.387	RS
0.00229	0.00038	16.50	10.825	0.255	0.355	99.390	RS
0.00191	0.00018	9.50	12.109	0.257	0.311	99.432	RS
0.00212	0	0	11.614	0.302	0.302	99.396	RS

The 26 other points corresponding to excess of R were deducted from mirror projection due to symmetry along racemic compositions in enantiomeric systems

**Table S5:** Comparison of four solubility values variation for pure R and S solubilities and S-MA with UV-CD spectroscopy and gravimetry methods.

	UV-CD spectroscopy		Gravimetry
	X (% mol)	Concentration (mg/mL)	
Pure R and S	0.889	29.218	-
	0.924	30.383	30.438
	0.935	30.756	30.981
	0.986	32.457	32.207
Average	<b>0.933</b>	<b>30.703</b>	<b>31.209</b>
Standard deviation	0.035	1.161	0.734
Pure S-MA	4.103	124.699	-
	4.076	123.861	121.052
	4.054	123.251	124.604
	3.985	120.961	119.771
Average	<b>4.054</b>	<b>123.193</b>	<b>121.809</b>
Standard deviation	0.044	1.387	2.044

### S3.2 – Isothermal ternary system between enantiomer S and S-SMA

**Table S6:** Data used for the ternary phase diagram S/S-MA/MeCN at 9°C.

Model prediction from UV-CD		Dilution	Final liquid composition (molar fraction)			Solid
$x_S$ in diluted solution	$x_{S-MA}$ in diluted solution	Dilution ratio	$X_S$ (%)	$X_{S-MA}$ (%)	$X_{MeCN}$ (%)	Solid phase(s) in suspension (XRPD)
0.00403	0.00000	9.237	0.924	0.000	99.083	S
0.00405	0.00122	11.974	1.229	0.414	98.357	S
0.00462	0.00185	11.946	1.412	0.633	97.954	S
0.00295	0.00146	20.953	1.603	0.887	97.509	S
0.00307	0.00158	20.601	1.641	0.944	97.415	S
0.00172	0.00000	21.678	0.924	0.000	99.071	S
0.00173	0.00000	21.764	0.935	0.000	99.060	S
0.00186	0.00000	21.381	0.986	0.000	99.018	S
0.00096	0.00050	67.722	1.701	0.983	97.316	S
0.00105	0.00052	66.641	1.833	1.016	97.152	S
0.00043	0.00378	42.511	0.502	4.984	94.514	S-MA
0.00028	0.00331	45.989	0.351	4.667	94.982	S-MA
0.00019	0.00256	58.420	0.307	4.575	95.118	S-MA

0.00003	0.00216	63.399	0.045	4.103	95.853	S-MA
0.00004	0.00212	63.946	0.063	4.076	95.861	S-MA
0.00006	0.00173	78.056	0.121	4.054	95.825	S-MA
0.00003	0.00204	65.176	0.053	3.984	95.962	S-MA
0.00054	0.00307	59.035	0.903	5.786	93.311	S-MA
0.00064	0.00316	58.974	1.082	6.026	92.892	S-MA
0.00059	0.00299	60.309	1.016	5.778	93.206	S-MA
0.00097	0.00420	45.585	1.293	6.257	92.449	S-MA
0.00074	0.00303	64.972	1.405	6.486	92.109	S-MA
0.00074	0.00315	61.701	1.338	6.379	92.283	S-MA
0.00105	0.00396	51.485	1.603	6.786	91.611	S-MA
0.00098	0.00359	59.026	1.739	7.132	91.130	S-MA
0.00101	0.00104	49.702	1.317	1.512	97.171	S:S-MA
0.00101	0.00244	52.329	1.477	3.981	94.542	S:S-MA
0.00078	0.00215	62.629	1.369	4.207	94.423	S:S-MA
0.00088	0.00253	56.878	1.414	4.530	94.055	S:S-MA
0.00106	0.00327	47.867	1.446	4.990	93.564	S:S-MA
0.00120	0.00371	42.160	1.444	4.980	93.576	S:S-MA
0.00110	0.00345	46.829	1.476	5.164	93.360	S:S-MA
0.00090	0.00287	57.190	1.479	5.271	93.250	S:S-MA
0.00114	0.00372	46.580	1.534	5.617	92.849	S:S-MA
0.00119	0.00423	44.496	1.554	6.169	92.278	S:S-MA
0.00119	0.00422	47.378	1.678	6.646	91.676	S:S-MA
0.00102	0.00360	56.960	1.733	6.864	91.403	S:S-MA
0.00119	0.00421	48.618	1.726	6.842	91.432	S:S-MA
0.00100	0.00352	58.655	1.766	6.930	91.304	S:S-MA
0.00129	0.00454	45.573	1.764	6.947	91.289	S:S-MA
0.00109	0.00358	49.021	1.545	5.694	92.761	S:S-MA
0.00112	0.00367	46.113	1.491	5.456	93.053	S:S-MA
0.00116	0.00401	48.195	1.650	6.380	91.970	S:S-MA
0.00130	0.00089	49.903	1.710	1.309	96.981	S:S-MA
0.00125	0.00075	62.757	2.086	1.397	96.516	S:S-MA
0.00104	0.00069	67.882	1.872	1.386	96.741	S:S-MA
0.00102	0.00074	64.592	1.735	1.409	96.855	S:S-MA
0.00087	0.00079	68.930	1.575	1.608	96.817	S:S-MA
0.00085	0.00094	63.791	1.425	1.768	96.807	S:S-MA
0.00081	0.00107	68.101	1.464	2.174	96.361	S:S-MA
0.00073	0.00117	61.931	1.191	2.142	96.666	S:S-MA
0.00092	0.00165	52.348	1.297	2.596	96.107	S:S-MA
0.00077	0.00156	60.033	1.239	2.816	95.946	S:S-MA
0.00080	0.00178	58.983	1.279	3.190	95.532	S:S-MA
0.00117	0.00066	63.977	1.974	1.253	96.773	S + S:S-MA

### S3.3 – Isothermal ternary system between enantiomer R and S-MA

**Table S7:** Data used for the ternary phase diagram R/S-MA/MeCN at 9°C.

Model prediction from UV-CD		Dilution	Final liquid composition (molar fraction)			Solid
$x_R$ in diluted solution	$x_{S-MA}$ in diluted solution	Dilution ratio	$X_R$ (%)	$X_{S-MA}$ (%)	$X_{MeCN}$ (%)	Solid phase(s) in suspension (XRPD)
0.00094	0.00011	53.036	1.262	0.168	98.571	R
0.00109	0.00026	51.026	1.411	0.379	98.211	R
0.00091	0.00036	89.046	2.133	0.935	96.932	R
0.00103	0.00047	87.759	2.424	1.240	96.336	R
0.00124	0.00072	83.848	2.860	1.865	95.274	R
0.00079	0.00048	163.125	3.695	2.477	93.827	R
0.00130	0.00088	110.166	4.209	3.199	92.592	R
0.00122	0.00086	133.803	4.968	3.940	91.092	R
0.00101	0.00079	178.077	5.719	4.967	89.313	R
0.00133	0.00106	153.884	6.825	6.054	87.121	R
0.00150	0.00125	143.384	7.332	6.861	85.808	R
0.00117	0.00103	190.982	7.878	7.737	84.385	R
0.00125	0.00116	214.444	10.525	10.937	78.537	R
0.00128	0.00109	231.981	12.150	11.580	76.270	R
0.00126	0.00106	246.714	13.073	12.280	74.647	R
0.00151	0.00142	196.486	12.486	13.146	74.368	R
0.00155	0.00139	210.004	14.561	14.624	70.815	R
0.00150	0.00138	225.100	15.800	16.276	67.925	R
0.00142	0.00129	229.829	14.755	14.985	70.260	R
0.00078	0.00147	218.602	6.469	13.668	79.862	S-MA
0.00068	0.00135	234.158	5.934	13.177	80.889	S-MA
0.00071	0.00161	180.174	4.469	11.307	84.224	S-MA
0.00083	0.00214	124.180	3.413	9.862	86.726	S-MA
0.00053	0.00149	163.260	2.760	8.686	88.554	S-MA
0.00062	0.00222	95.137	1.777	7.096	91.127	S-MA
0.00050	0.00207	93.682	1.363	6.344	92.294	S-MA
0.00029	0.00275	59.964	0.491	5.127	94.382	S-MA
0.00017	0.00242	65.795	0.308	4.911	94.781	S-MA
			Suspension composition			
			19.914	26.145	53.942	No solid
			22.539	29.862	47.599	No solid
			24.740	32.748	42.511	S-MA
			26.783	35.136	38.080	S-MA
			29.847	39.608	30.545	S-MA

### S3.4 – Quaternary phase diagram R/S/S-MA/MeCN

**Table S8:** Data used for the quaternary phase diagram R/S/S-MA/MeCN at 9°C (inside of the tetrahedron).

Model prediction from UV-CD			Dilution	Final liquid composition (molar fraction)				Solubility surface projection (molar fraction)			Solid phase(s) in suspension (XRPD)
$x_R$ in diluted solution	$x_S$ in diluted solution	$x_{S-MA}$ in diluted solution	Dilution ratio	$x_R$ (%)	$x_S$ (%)	$x_{S-MA}$ (%)	$x_{MeCN}$ (%)	$x_S$ (%)	$x_{S-MA}$ (%)	$x_R$ (%)	XRPD
0.00087	0.00087	0.00177	48.943	1.171	1.174	2.675	94.980	23.386	53.281	23.334	RS
0.00055	0.00052	0.00102	70.578	1.045	1.002	2.179	95.774	23.706	51.572	24.723	RS
0.00041	0.00038	0.00066	76.957	0.828	0.773	1.493	96.906	24.983	48.256	26.761	RS
0.00062	0.00057	0.00094	42.213	0.679	0.625	1.152	97.544	25.458	46.895	27.647	RS
0.00046	0.00050	0.00050	42.664	0.498	0.538	0.599	98.365	32.895	36.643	30.462	RS
0.00020	0.00116	0.00050	46.746	0.237	1.402	0.676	97.685	60.564	29.215	10.221	S+RS
0.00020	0.00120	0.00042	40.499	0.212	1.241	0.483	98.065	64.121	24.932	10.948	S+RS
0.00020	0.00125	0.00044	38.312	0.194	1.224	0.485	98.098	64.332	25.488	10.181	S+RS
0.00018	0.00131	0.00045	37.799	0.177	1.267	0.491	98.064	65.477	25.381	9.141	S+RS
0.00026	0.00154	0.00080	39.679	0.274	1.602	0.927	97.198	57.169	33.065	9.766	S+RS
0.00027	0.00169	0.00095	38.027	0.268	1.692	1.068	96.972	55.871	35.275	8.854	S+RS
0.00021	0.00144	0.00074	43.277	0.234	1.632	0.932	97.201	58.321	33.307	8.372	S+RS
0.00020	0.00122	0.00077	62.745	0.336	2.050	1.455	96.159	53.376	37.875	8.748	S+RS
0.00021	0.00131	0.00081	55.686	0.310	1.947	1.347	96.397	54.032	37.377	8.591	S+RS
0.00022	0.00135	0.00088	53.674	0.317	1.942	1.408	96.333	52.964	38.385	8.651	S:S-MA+S
0.00018	0.00093	0.00069	74.849	0.364	1.860	1.539	96.237	49.426	40.895	9.678	S:S-MA+RS
0.00020	0.00110	0.00068	68.658	0.377	2.023	1.411	96.190	53.092	37.023	9.885	S:S-MA
0.00016	0.00119	0.00073	63.320	0.264	2.019	1.379	96.338	55.140	37.658	7.201	S:S-MA
0.00029	0.00089	0.00090	65.956	0.515	1.575	1.785	96.125	40.648	46.059	13.293	S:S-MA
0.00021	0.00099	0.00082	64.593	0.355	1.704	1.587	96.355	46.744	43.521	9.735	S:S-MA
0.00071	0.00090	0.00259	59.571	1.259	1.589	5.118	92.034	19.944	64.247	15.809	S:S-MA

0.0004 1	0.0009 3	0.0021 0	59.825	0.700	1.589	4.000	93.711	25.275	63.601	11.123	S:S- MA
0.0003 5	0.0008 1	0.0028 9	65.234	0.691	1.590	6.315	91.404	18.502	73.458	8.040	S:S- MA
0.0004 0	0.0010 6	0.0039 8	54.905	0.688	1.799	7.561	89.952	17.909	75.247	6.844	S:S- MA
0.0003 8	0.0004 1	0.0033 0	57.816	0.649	0.691	6.227	92.434	9.131	82.297	8.572	S-MA
0.0006 4	0.0006 8	0.0037 7	60.716	1.211	1.295	7.999	89.494	12.328	76.140	11.531	S-MA
0.0009 0	0.0009 6	0.0033 3	65.173	1.882	2.005	7.809	88.305	17.143	66.769	16.088	S:S- MA
0.0015 0	0.0012 2	0.0036 9	48.852	2.303	1.877	6.336	89.484	17.847	60.253	21.900	S:S- MA
0.0002 4	0.0009 4	0.0003 3	39.949	0.238	0.951	0.369	98.443	61.046	23.689	15.265	RS
0.0002 2	0.0014 0	0.0003 9	38.838	0.221	1.395	0.437	97.947	67.927	21.304	10.768	S+RS
0.0002 4	0.0013 2	0.0003 5	38.104	0.231	1.286	0.383	98.100	67.666	20.158	12.177	S+RS
0.0002 0	0.0012 9	0.0003 8	40.246	0.209	1.322	0.440	98.028	67.071	22.328	10.601	S+RS
0.0002 0	0.0014 0	0.0004 7	36.829	0.188	1.321	0.495	97.995	65.905	24.699	9.396	S
0.0003 2	0.0013 2	0.0005 5	43.854	0.370	1.510	0.705	97.415	58.421	27.269	14.310	RS
0.0003 4	0.0011 0	0.0007 9	39.231	0.349	1.110	0.890	97.651	47.265	37.885	14.850	RS
0.0002 8	0.0016 0	0.0006 8	38.293	0.278	1.595	0.759	97.368	60.604	28.837	10.559	RS
0.0002 4	0.0016 3	0.0008 0	40.602	0.256	1.735	0.953	97.057	58.935	32.374	8.691	S
0.0004 2	0.0016 0	0.0010 6	35.765	0.394	1.506	1.118	96.982	49.913	37.030	13.057	RS
0.0002 9	0.0018 0	0.0011 2	44.681	0.356	2.176	1.513	95.955	53.799	37.400	8.802	S+RS
0.0006 2	0.0013 1	0.0013 9	40.116	0.667	1.412	1.672	96.249	37.645	44.577	17.778	RS
0.0004 1	0.0021 7	0.0013 7	36.006	0.394	2.110	1.487	96.009	52.871	37.252	9.876	RS
0.0002 6	0.0020 0	0.0011 9	39.848	0.274	2.147	1.426	96.153	55.807	37.064	7.129	S:S- MA+S
0.0003 4	0.0009 5	0.0009 1	63.642	0.581	1.626	1.753	96.040	41.070	44.258	14.671	RS
0.0003 4	0.0018 8	0.0011 6	41.019	0.371	2.075	1.427	96.127	53.574	36.851	9.575	S:S- MA+R S
0.0006 5	0.0009 4	0.0014 1	52.943	0.937	1.364	2.284	95.415	29.749	49.808	20.444	RS
0.0003 4	0.0005 7	0.0010 1	65.902	0.594	0.999	1.988	96.419	27.906	55.507	16.587	RS
0.0007 8	0.0010 6	0.0018 4	52.099	1.146	1.560	3.012	94.282	27.285	52.674	20.041	RS
0.0006 8	0.0010 8	0.0017 1	55.322	1.061	1.689	2.983	94.267	29.461	52.038	18.502	S:S- MA
0.0002 4	0.0010 2	0.0013 6	53.308	0.348	1.457	2.181	96.015	36.563	54.714	8.723	S:S- MA
0.0009 4	0.0011 4	0.0022 7	49.959	1.344	1.631	3.647	93.379	24.628	55.080	20.292	S:S- MA

0.0009 2	0.0010 6	0.0033 4	51.472	1.432	1.654	5.816	91.098	18.582	65.330	16.088	S:S- MA
0.0005 7	0.0010 8	0.0038 9	43.588	0.725	1.377	5.562	92.337	17.968	72.575	9.457	S:S- MA
0.0011 2	0.0012 2	0.0039 8	49.605	1.742	1.896	6.928	89.434	17.948	65.565	16.487	S:S- MA
0.0007 7	0.0009 8	0.0040 8	53.499	1.285	1.644	7.643	89.428	15.546	72.297	12.157	S:S- MA
0.0005 7	0.0010 7	0.0046 8	51.981	0.937	1.777	8.657	88.628	15.630	76.126	8.244	S-MA
0.0005 4	0.0010 2	0.0046 9	47.279	0.780	1.491	7.641	90.087	15.043	77.085	7.872	S-MA
0.0002 8	0.0001 2	0.0011 7	139.523	1.109	0.472	5.273	93.145	6.892	76.927	16.181	S-MA
0.0004 5	0.0001 3	0.0015 8	141.129	1.971	0.575	7.755	89.699	5.581	75.285	19.133	S-MA
0.0003 7	0.0001 8	0.0015 2	146.910	1.673	0.837	7.773	89.717	8.141	75.587	16.272	S-MA
0.0007 2	0.0002 7	0.0023 7	112.468	2.714	1.015	9.967	86.304	7.412	72.772	19.817	S-MA
0.0003 9	0.0002 4	0.0014 2	181.283	2.359	1.430	9.535	86.675	10.734	71.560	17.706	S-MA
0.0005 8	0.0001 8	0.0015 3	189.884	3.945	1.205	11.554	83.296	7.214	69.170	23.616	S-MA
0.0005 0	0.0002 4	0.0014 5	197.506	3.517	1.672	11.368	83.444	10.096	68.663	21.241	S-MA
0.0004 7	0.0003 3	0.0016 9	170.410	2.784	1.999	11.301	83.915	12.431	70.260	17.309	S-MA
0.0007 9	0.0003 2	0.0019 3	184.459	6.030	2.456	16.468	75.046	9.843	65.994	24.163	S-MA
0.0006 0	0.0003 6	0.0016 2	223.500	5.683	3.373	16.999	73.945	12.945	65.242	21.813	S-MA
0.0004 6	0.0003 1	0.0011 5	257.884	4.582	3.097	12.746	79.576	15.162	62.404	22.434	S:S- MA
0.0008 4	0.0003 3	0.0014 2	252.583	9.991	3.924	18.901	67.184	11.958	57.596	30.447	S:S- MA
0.0009 7	0.0004 2	0.0018 6	188.424	8.122	3.544	17.382	70.952	12.199	59.840	27.962	S:S- MA
0.0009 7	0.0005 0	0.0020 2	157.046	6.177	3.195	14.408	76.220	13.436	60.589	25.975	S:S- MA
0.0007 3	0.0004 5	0.0014 1	169.992	4.461	2.736	9.650	83.153	16.242	57.281	26.478	S:S- MA
0.0011 0	0.0004 4	0.0017 2	190.280	9.336	3.735	16.402	70.527	12.673	55.650	31.677	S:S- MA
0.0009 8	0.0003 9	0.0016 8	195.249	8.317	3.272	15.876	72.534	11.915	57.804	30.281	S:S- MA
0.0007 9	0.0003 7	0.0015 1	193.166	5.986	2.813	12.718	78.483	13.074	59.109	27.818	S:S- MA
0.0005 6	0.0003 6	0.0012 1	211.423	4.250	2.744	10.307	82.698	15.862	59.575	24.563	S:S- MA
0.0012 3	0.0003 9	0.0016 2	189.678	10.394	3.252	15.297	71.056	11.237	52.852	35.911	RS
0.0009 8	0.0003 6	0.0014 4	214.768	9.137	3.376	14.960	72.527	12.287	54.455	33.258	S:S- MA
0.0010 5	0.0004 2	0.0015 8	190.103	8.416	3.356	14.221	74.007	12.913	54.709	32.379	S:S- MA
0.0008 6	0.0004 4	0.0014 0	163.365	5.079	2.591	9.221	83.109	15.338	54.595	30.067	S:S- MA
0.0006 9	0.0003 8	0.0011 1	162.698	3.695	2.035	6.598	87.671	16.506	53.521	29.973	S:S- MA

0.0015 0	0.0003 2	0.0016 9	145.224	8.476	1.818	10.671	79.036	8.672	50.899	40.429	No solid
0.0014 5	0.0004 1	0.0018 7	121.134	6.392	1.797	9.197	82.615	10.334	52.901	36.765	RS
0.0009 0	0.0004 0	0.0013 7	155.469	4.861	2.185	8.282	84.672	14.253	54.033	31.714	RS
0.0006 2	0.0003 4	0.0009 9	165.274	3.276	1.778	5.808	89.138	16.371	53.471	30.159	S:S- MA+R S
0.0004 5	0.0004 5	0.0001 4	39.876	0.448	0.442	0.160	98.950	42.131	15.194	42.674	RS
0.0003 8	0.0003 8	0.0002 4	53.510	0.509	0.508	0.361	98.622	36.854	26.195	36.951	RS
0.0005 1	0.0004 7	0.0003 2	45.035	0.574	0.536	0.407	98.483	35.312	26.854	37.834	RS
0.0006 3	0.0005 9	0.0007 7	45.195	0.735	0.684	1.010	97.570	28.166	41.575	30.259	RS
0.0005 7	0.0005 4	0.0007 7	48.477	0.714	0.679	1.085	97.521	27.403	43.779	28.818	RS
0.0006 8	0.0006 6	0.0010 7	46.267	0.827	0.808	1.460	96.905	26.099	47.170	26.732	RS
0.0002 7	0.0008 9	0.0001 9	44.731	0.302	1.000	0.237	98.461	64.989	15.377	19.634	RS
0.0002 0	0.0009 4	0.0001 0	47.574	0.242	1.132	0.140	98.485	74.722	9.273	16.005	RS
0.0001 7	0.0010 8	0.0001 7	44.796	0.192	1.224	0.221	98.363	74.761	13.504	11.734	S+RS
0.0001 7	0.0010 8	0.0001 8	45.541	0.192	1.243	0.229	98.336	74.708	13.783	11.509	S+RS
0.0001 5	0.0010 7	0.0000 8	48.212	0.189	1.305	0.103	98.404	81.751	6.431	11.818	S+RS
0.0001 7	0.0011 6	0.0001 7	47.046	0.203	1.390	0.230	98.176	76.237	12.624	11.139	S+RS
0.0001 5	0.0010 4	0.0001 0	45.235	0.170	1.190	0.125	98.515	80.129	8.406	11.465	S+RS
0.0001 7	0.0011 0	0.0001 4	44.706	0.188	1.245	0.178	98.389	77.260	11.076	11.664	S+RS
0.0001 2	0.0009 8	0.0001 1	49.294	0.150	1.218	0.159	98.473	79.770	10.398	9.832	S
0.0001 5	0.0012 5	0.0004 2	45.802	0.173	1.469	0.559	97.800	66.759	25.394	7.847	S
0.0001 0	0.0014 9	0.0006 5	47.349	0.118	1.846	0.903	97.133	64.380	31.500	4.121	S
0.0001 1	0.0017 1	0.0008 3	45.177	0.126	2.043	1.106	96.725	62.379	33.780	3.841	S
0.0001 2	0.0017 1	0.0010 3	47.552	0.153	2.188	1.475	96.183	57.339	38.652	4.009	S
0.0001 8	0.0013 2	0.0003 2	44.499	0.202	1.512	0.415	97.871	71.023	19.491	9.486	S+RS
0.0003 6	0.0007 7	0.0004 6	45.547	0.414	0.899	0.599	98.088	47.026	31.342	21.632	RS
0.0002 6	0.0013 8	0.0007 3	42.597	0.285	1.536	0.906	97.273	56.316	33.215	10.469	RS
0.0004 6	0.0008 8	0.0009 0	45.994	0.555	1.054	1.212	97.179	37.365	42.972	19.663	RS
0.0001 6	0.0016 9	0.0011 2	51.500	0.219	2.363	1.757	95.661	54.454	40.500	5.046	S:S- MA+S
0.0001 2	0.0016 0	0.0010 6	52.515	0.175	2.274	1.687	95.865	54.980	40.794	4.226	S:S- MA+S



0.0001 5	0.0017 9	0.0012 9	49.160	0.200	2.411	1.937	95.452	53.018	42.590	4.392	S:S- MA+S
0.0001 5	0.0018 7	0.0013 7	49.325	0.211	2.537	2.082	95.171	52.527	43.110	4.363	S:S- MA+S
0.0001 1	0.0018 5	0.0013 4	51.247	0.158	2.623	2.121	95.098	53.514	43.273	3.214	S:S- MA+S
0.0010 4	0.0001 4	0.0003 4	54.444	1.458	0.202	0.528	97.812	9.211	24.135	66.654	R+RS
0.0011 0	0.0001 8	0.0002 6	48.083	1.355	0.216	0.355	98.074	11.212	18.452	70.336	R+RS
0.0009 8	0.0001 6	0.0002 8	52.079	1.310	0.216	0.423	98.051	11.108	21.680	67.212	R+RS
0.0009 0	0.0002 1	0.0002 1	48.209	1.095	0.256	0.288	98.360	15.636	17.574	66.790	RS
0.0009 0	0.0001 3	0.0005 1	89.075	2.150	0.322	1.364	96.163	8.396	35.563	56.040	R+RS
0.0006 0	0.0001 2	0.0002 9	108.553	1.714	0.355	0.927	97.004	11.841	30.936	57.223	R+RS
0.0006 6	0.0001 5	0.0002 9	97.926	1.686	0.384	0.842	97.088	13.202	28.903	57.895	R+RS
0.0005 6	0.0001 6	0.0003 3	93.800	1.359	0.388	0.893	97.360	14.684	33.836	51.480	RS
0.0008 5	0.0001 3	0.0004 6	99.596	2.276	0.361	1.392	95.972	8.959	34.552	56.490	R+RS
0.0008 4	0.0001 4	0.0004 7	99.598	2.256	0.367	1.400	95.977	9.120	34.800	56.080	R+RS
0.0009 9	0.0001 6	0.0005 7	82.983	2.216	0.351	1.432	96.001	8.777	35.802	55.421	R+RS
0.0008 6	0.0002 2	0.0006 8	54.739	1.228	0.311	1.081	97.380	11.875	41.265	46.860	RS
0.0008 0	0.0001 3	0.0005 7	132.948	3.011	0.472	2.389	94.128	8.033	40.689	51.278	R+RS
0.0007 7	0.0001 6	0.0005 8	140.770	3.089	0.633	2.640	93.638	9.950	41.496	48.554	R+RS
0.0007 3	0.0001 3	0.0005 4	140.845	2.898	0.535	2.422	94.144	9.144	41.362	49.494	RS
0.0010 3	0.0001 5	0.0008 5	121.991	3.701	0.526	3.430	92.344	6.867	44.794	48.339	R+RS
0.0009 0	0.0001 4	0.0006 6	151.953	4.063	0.641	3.348	91.948	7.965	41.576	50.459	R+RS
0.0010 6	0.0002 0	0.0008 6	119.881	3.774	0.717	3.453	92.057	9.022	43.469	47.509	RS
0.0010 2	0.0001 3	0.0008 1	167.964	5.469	0.672	4.889	88.970	6.096	44.323	49.581	R+RS
0.0009 1	0.0001 4	0.0007 4	183.369	5.339	0.850	4.863	88.948	7.691	44.003	48.306	RS
0.0006 8	0.0003 6	0.0009 7	142.777	2.993	1.560	4.737	90.710	16.791	50.993	32.217	RS
0.0011 5	0.0001 4	0.0009 9	171.902	6.745	0.793	6.451	86.012	5.668	46.115	48.217	R+RS
0.0006 9	0.0001 1	0.0005 9	287.405	6.847	1.125	6.589	85.440	7.724	45.252	47.024	RS
0.0005 8	0.0002 2	0.0007 4	243.135	4.702	1.807	6.704	86.786	13.677	50.736	35.587	RS
0.0011 5	0.0001 5	0.0010 8	184.329	7.575	1.018	8.017	83.390	6.130	48.268	45.602	RS
0.0008 5	0.0002 5	0.0010 3	202.866	6.135	1.811	8.288	83.766	11.153	51.055	37.792	RS
0.0015 4	0.0002 1	0.0016 1	173.935	11.413	1.575	13.348	73.664	5.982	50.683	43.335	R+RS

0.0010 3	0.0002 7	0.0012 6	189.507	7.360	1.937	10.053	80.650	10.012	51.952	38.036	RS
0.0007 2	0.0005 7	0.0010 5	85.093	1.722	1.361	2.829	94.088	23.018	47.854	29.128	RS
0.0007 1	0.0005 7	0.0011 9	84.666	1.720	1.376	3.220	93.684	21.790	50.982	27.228	S:S- MA+R S
0.0007 8	0.0006 1	0.0012 2	95.143	2.202	1.712	3.843	92.243	22.070	49.543	28.387	RS
0.0010 2	0.0007 5	0.0016 8	75.951	2.316	1.713	4.278	91.694	20.620	51.499	27.881	S:S- MA+R S
0.0007 8	0.0004 9	0.0013 6	142.924	3.740	2.338	7.280	86.642	17.500	54.504	27.996	S:S- MA
0.0007 9	0.0004 6	0.0012 4	168.396	4.641	2.740	8.191	84.428	17.594	52.601	29.804	S:S- MA+R S
0.0007 6	0.0004 0	0.0016 2	159.830	4.356	2.315	10.423	82.906	13.542	60.973	25.485	S:S- MA
0.0008 0	0.0005 0	0.0016 7	159.326	4.713	2.989	11.069	81.229	15.924	58.968	25.109	S:S- MA
0.0008 8	0.0006 6	0.0026 5	109.643	3.527	2.645	11.883	81.944	14.652	65.813	19.536	S:S- MA
0.0009 3	0.0006 8	0.0028 5	103.072	3.513	2.555	12.016	81.916	14.130	66.447	19.423	S:S- MA+S- MA
0.0004 5	0.0003 7	0.0022 4	97.896	1.362	1.136	7.598	89.903	11.254	75.255	13.491	S-MA
0.0003 8	0.0003 2	0.0019 3	106.492	1.231	1.021	6.987	90.761	11.050	75.623	13.327	S-MA
0.0000 7	0.0001 1	0.0015 7	107.460	0.211	0.333	5.280	94.176	5.711	90.657	3.631	S-MA
0.0003 6	0.0001 3	0.0017 6	103.977	1.078	0.394	5.963	92.565	5.295	80.203	14.501	S-MA
0.0007 1	0.0004 6	0.0010 7	113.836	2.413	1.552	4.057	91.977	19.349	50.571	30.080	S:S- MA+R S
0.0008 7	0.0005 0	0.0013 0	109.018	2.926	1.674	4.882	90.518	17.650	51.493	30.857	S:S- MA+R S
0.0009 8	0.0005 8	0.0015 1	100.426	3.086	1.819	5.311	89.785	17.804	51.989	30.207	S:S- MA+R S
0.0011 3	0.0005 6	0.0017 4	118.247	4.626	2.277	7.952	85.145	15.330	53.527	31.142	S:S- MA+R S
0.0011 3	0.0004 3	0.0016 0	141.261	5.760	2.199	9.132	82.909	12.866	53.432	33.702	RS
0.0012 4	0.0003 6	0.0016 7	210.002	12.849	3.724	19.352	64.075	10.365	53.867	35.767	S:S- MA
0.0011 4	0.0002 9	0.0015 3	236.452	13.571	3.445	20.367	62.618	9.215	54.482	36.303	S:S- MA
0.0013 8	0.0003 8	0.0017 4	216.332	16.505	4.545	23.281	55.668	10.252	52.517	37.231	S:S- MA
0.0013 4	0.0003 5	0.0018 3	200.696	13.701	3.540	20.886	61.873	9.285	54.779	35.936	S:S- MA
0.0009 2	0.0003 5	0.0012 3	290.681	13.914	5.246	20.925	59.914	13.088	52.201	34.711	S:S- MA
0.0012 3	0.0004 7	0.0017 6	203.680	12.722	4.840	20.341	62.097	12.769	53.665	33.566	S:S- MA

0.0008 6	0.0003 6	0.0012 4	283.132	12.203	5.098	19.672	63.028	13.789	53.207	33.005	S:S- MA
0.0014 8	0.0003 5	0.0018 6	211.656	17.917	4.191	25.276	52.616	8.844	53.343	37.813	S:S- MA
0.0014 0	0.0003 6	0.0019 1	195.214	14.113	3.629	21.540	60.717	9.238	54.834	35.927	S:S- MA

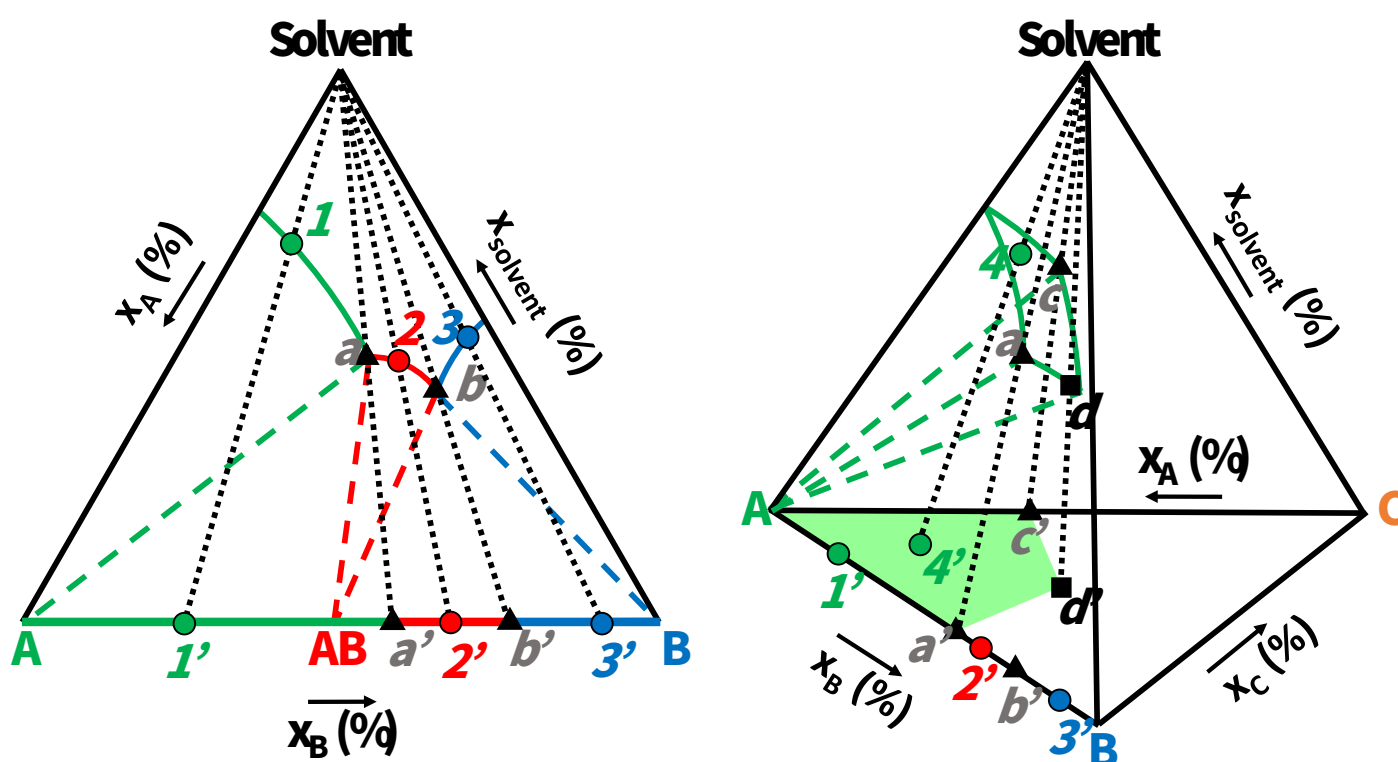


**Figure S15:** Left: projection of solubility curves (solid lines) of A (green), AB (red) and B (blue) on solvent-free axis AB in the isothermal ternary phase diagram A/B/Solvent. Dotted lines connect solubility compositions (1, 2, 3, a, b) to their solvent-free equivalent (1', 2', 3', a', b'). Dashed lines represent the boundaries of phase stability domains. Eutectic compositions a and b (black triangles) represent the liquid phase composition of a suspension equilibrating in a triphasic domain. Right: projection of solubility surface of A (green) on solvent-free surface ABC in the isothermal quaternary phase diagram A/B/C/Solvent. Dotted lines connect solubility compositions (4, a, c, d) to their solvent-free equivalent (4', a', c', d'). The data from the AB axis of the ternary phase diagram on the left are shown on the AB axis. Dashed lines represent the boundaries of the phase stability domain. The solubility surface of A is limited by solubility curves from ternaries A/B/Solvent and A/C/Solvent, and eutectic lines linking ternary eutectic compositions a and c (black triangles) to quaternary composition d (black square) involving A. Quaternary composition d represents the liquid phase composition of a suspension equilibrating in a quadriphasic domain.

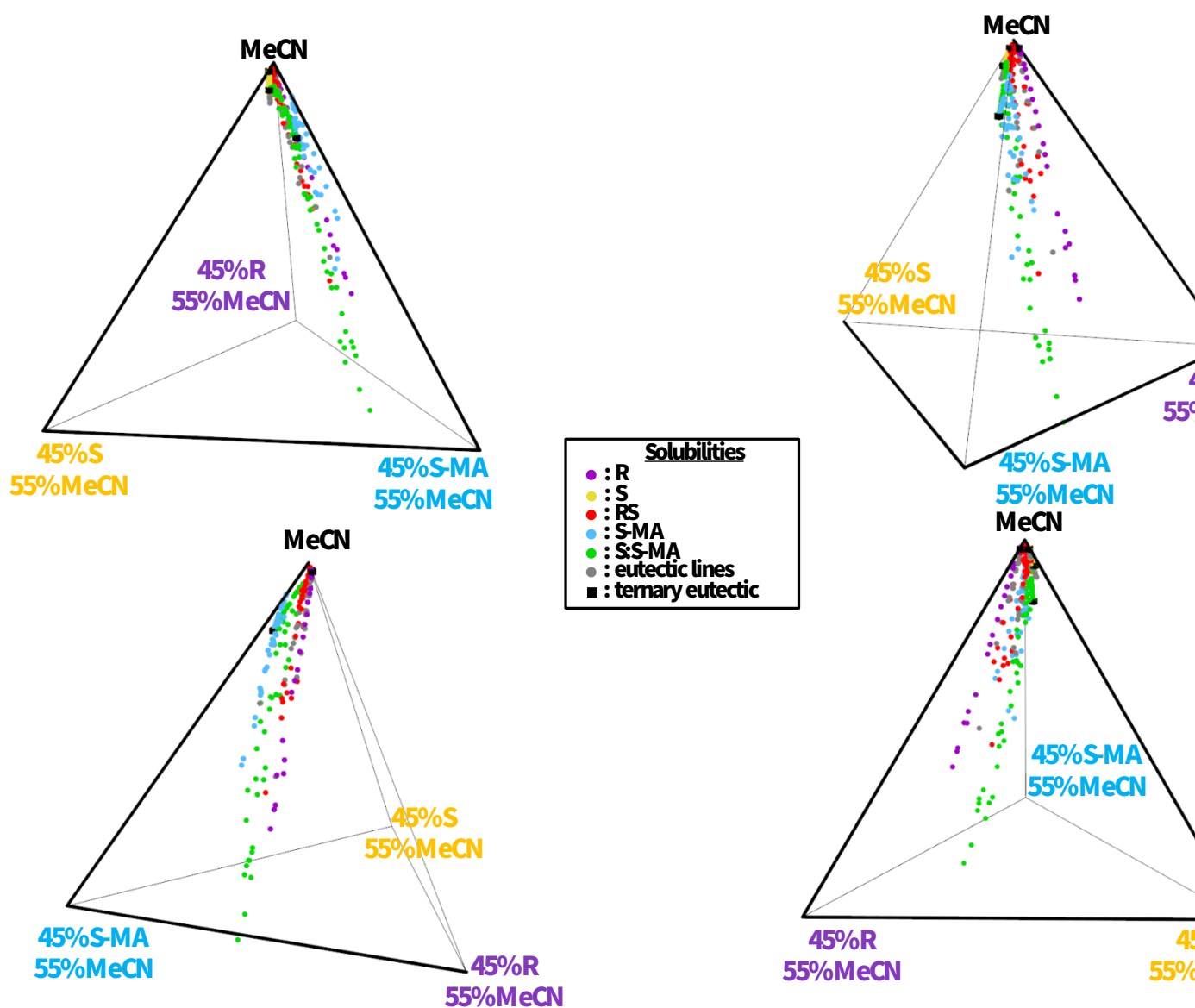


**Figure S16:** Zoom in the 55% MeCN to 100% MeCN tetrahedron region of the R/S/S-MA/MeCN quaternary phase diagram, with different viewing angles.

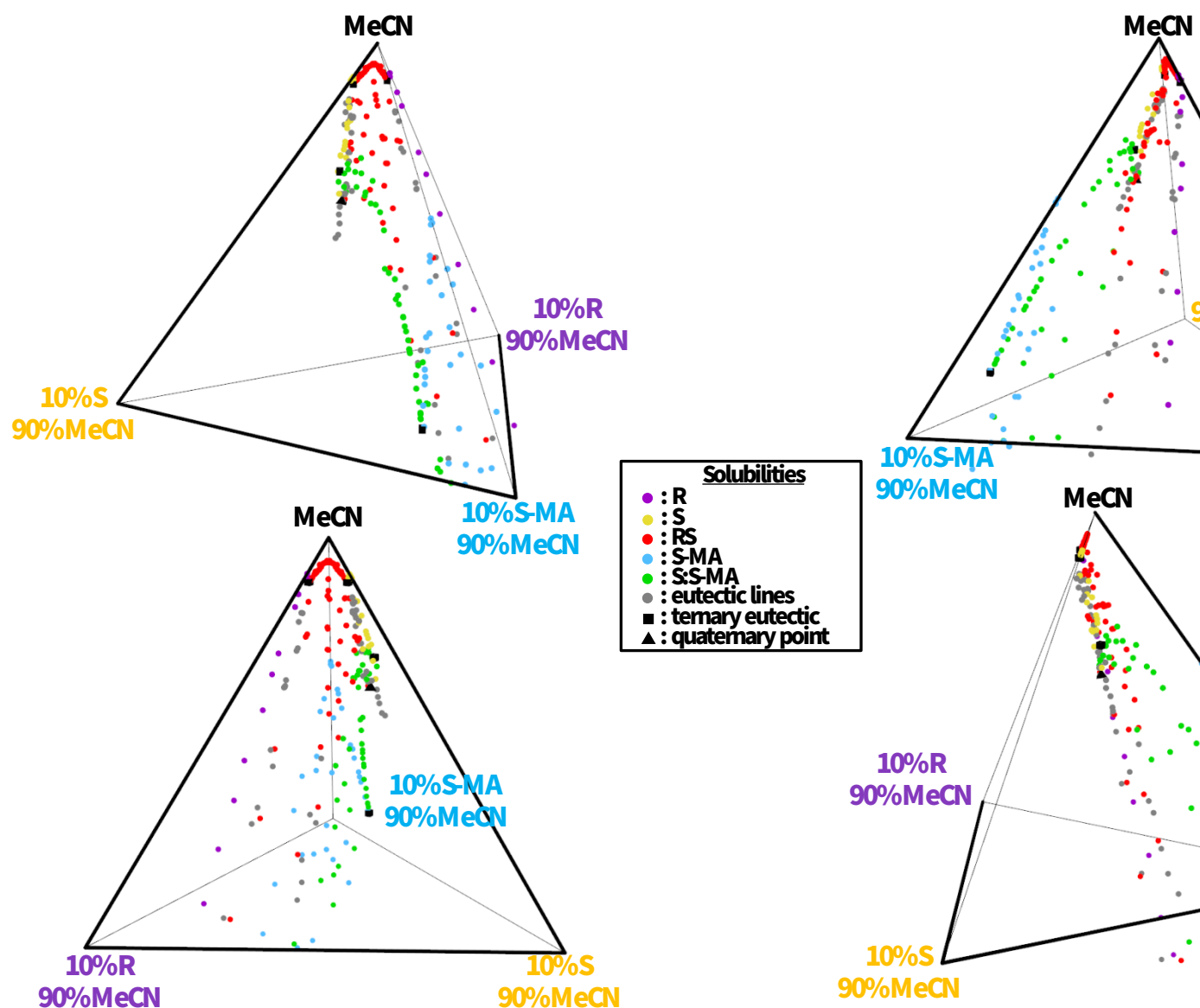


**Figure S17:** Zoom in the 90% MeCN to 100% MeCN tetrahedron region of the R/S/S-MA/MeCN quaternary phase diagram at 9°C, with different viewing angles.